A&A 570, A33 (2014)
DOI: 10.1051/0004-6361/201423669

Astronomy & Astrophysics

Discovery of binarity, spectroscopic frequency analysis, and mode identification of the δ Scuti star 4 CVn*,**,***

V. S. Schmid[1,★★★★], N. Themeßl[2,3], M. Breger[3,4], P. Degroote[1,†], C. Aerts[1,5], P. G. Beck[1,6], A. Tkachenko[1,†], T. Van Reeth[1], S. Bloemen[5], J. Debosscher[1], B. G. Castanheira[4], B. E. McArthur[4], P. I. Pápics[1], V. Fritz[3], and R. E. Falcon[4]

[1] Institute of Astronomy, KU Leuven, Celestijnenlaan 200D, 3001 Leuven, Belgium
e-mail: valentina.schmid@ster.kuleuven.be
[2] Max-Planck Institut für Sonnensystemforschung, Justus-von-Liebig-Weg 3, 37077 Göttingen, Germany
[3] Department of Astrophysics, University of Vienna, Türkenschanzstraße 17, 1180 Vienna, Austria
[4] Department of Astronomy, University of Texas at Austin 2515 Speedway, Stop C1400 Austin, Texas 78712-1205, USA
[5] Department of Astrophysics/IMAPP, Radboud University Nijmegen, PO Box 9010, 6500 GL Nijmegen, The Netherlands
[6] Laboratoire AIM, CEA/DSM – CNRS – Université Denis Diderot – IRUF/SAp, 91191 Gif-sur-Yvette Cedex, France

Received 18 February 2014 / Accepted 10 July 2014

ABSTRACT

More than 40 years of ground-based photometric observations of the δ Sct star 4 CVn has revealed 18 independent oscillation frequencies, including radial as well as non-radial p-modes of low spherical degree $\ell \leq 2$. From 2008 to 2011, more than 2000 spectra were obtained at the 2.1 m Otto-Struve telescope at the McDonald Observatory. We present the analysis of the line-profile variations, based on the Fourier-parameter fit method, detected in the absorption lines of 4 CVn, which carry clear signatures of the pulsations. From a non-sinusoidal, periodic variation of the radial velocities, we discover that 4 CVn is an eccentric binary system with an orbital period $P_{\rm orb} = 124.44 \pm 0.03$ d and an eccentricity $e = 0.311 \pm 0.003$. We detect 20 oscillation frequencies, 9 of which previously unseen in photometric data; attempt mode identification for the two dominant modes, $f_1 = 7.3764$ d^{-1} and $f_2 = 5.8496$ d^{-1}; and determine the prograde or retrograde nature of 7 of the modes. The projected rotational velocity of the star, $v_{\rm eq} \sin i \simeq 106.7$ km s^{-1}, translates to a rotation rate of $v_{\rm eq}/v_{\rm crit} \geq 33\%$. This relatively high rotation rate hampers unique mode identification, since higher order effects of rotation are not included in the current methodology. We conclude that, in order to achieve unambiguous mode identification for 4 CVn, a complete description of rotation and the use of blended lines have to be included in mode-identification techniques.

Key words. techniques: spectroscopic – stars: variables: δ Scuti – stars: individual: 4 CVn – stars: fundamental parameters – binaries: spectroscopic

1. Introduction

In the Hertzsprung-Russell diagram the group of δ Sct pulsators is located in the classical instability strip. They are on or slightly above the main sequence moving toward the giant branch after the hydrogen in their cores is depleted. This evolutionary stage makes them interesting from an astrophysical point of view and important objects for asteroseismic studies, since their interior structures undergo large changes. Comprehensive reviews of δ Sct stars and of asteroseismology are given by Breger (2000a) and Aerts et al. (2010), respectively.

New advances in the field of A- and F-type stars were achieved by space-based telescopes, such as MOST (Walker et al. 2003), CoRoT (Auvergne et al. 2009), and most recently *Kepler* (Borucki et al. 2010), which provide high-precision time series photometry. For example, Antoci et al. (2011) reported the first detections of solar-like oscillations in a δ Sct star, and Murphy et al. (2013) presented a detailed asteroseismic study of an SX Phe star in a binary and also derived masses for both components. Grigahcène et al. (2010) and Uytterhoeven et al. (2011, and references therein) found that γ Dor/δ Sct hybrids are a much more common phenomenon than expected from ground-based observations. Nevertheless, extensive ground-based observing campaigns are still necessary. Differences between different passbands and variations occurring on very long timescales of years and decades are hidden in the white-light photometric data of space missions that are comparatively short-lived. High-precision spectroscopic observations allow us to study the features of stellar oscillations in line-profile variations (LPVs) and give important information on the abundances of stellar photospheres. In this paper we present the results of long-term spectroscopic observations of 4 CVn, one of the best studied δ Sct stars.

The star 4 CVn ($V = 6.04$ mag, $T_{\rm eff} = 6800 \pm 150$ K, $\log g = 3.34 \pm 0.20$, $\log L/L_\odot = 1.550 \pm 0.070$, $v_{\rm eq} \sin i \geq 120$ km s^{-1}; Lenz et al. 2010; Castanheira et al. 2008) has been observed photometrically for more than 40 years. The analysis of the

⋆ This paper includes data taken at The McDonald Observatory of The University of Texas at Austin.
⋆⋆ The software package FAMIAS, developed in the framework of the FP6 European Coordination Action HELAS (http://www.helas-eu.org/), has been used in this research.
⋆⋆⋆ Appendices are available in electronic form at http://www.aanda.org
⋆⋆⋆⋆ Aspirant Ph.D. Fellow, Fonds voor Wetenschappelijk Onderzoek – Vlaanderen (FWO), Belgium.
† Postdoctoral fellow of the Fonds voor Wetenschappelijk Onderzoek – Vlaanderen (FWO), Belgium.

Table 1. Photometric frequencies and amplitudes, and preliminary mode identification of 4 CVn.

	Frequency	Amplitude	ℓ	m
		y filter		
	d^{-1}	mmag		
ν_1	8.595	15.3	1	1
ν_2	7.375	11.6	1	–1
ν_3	5.048	10.7	1	–1
ν_4	6.117	9.2		
ν_5	5.851	10.1	2	1
ν_6	5.532	6.4	2	
ν_7	6.190	5.7		
ν_8	6.976	5.0	0	0
ν_9	4.749	3.2		
ν_{10}	7.552	3.3	1	
ν_{11}	6.750	0.9		
ν_{12}	6.440	1.6		
ν_{13}	5.986	0.8		
ν_{14}	7.896	0.8		
ν_{15}	5.134	0.8		
ν_{16}	5.314	0.8		
ν_{17}	6.404	0.4		
ν_{18}	6.680	0.2		

Notes. Frequencies and amplitudes taken from Breger et al. (1999). The ℓ values are based on multicolor photometry by Lenz et al. (2010) and the m values are the preliminary results of the spectroscopic mode identification of the 2008 data set by Castanheira et al. (2008), ignoring the binarity of the pulsator.

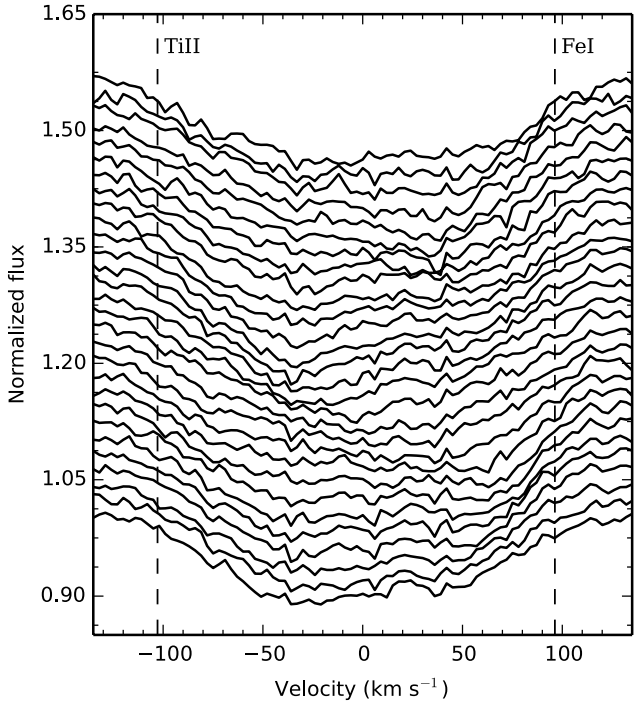

Fig. 1. Line-profile variations in the Fe II line at 4508.288 Å. The flux is normalized to 1 and is displayed with an offset. Shown are 29 spectra from the night of 31 March 2010. The vertical, dashed lines mark the metal lines Ti II at 4506.743 Å (−102.81 km s^{-1}) and Fe II at 4509.735 Å (96.29 km s^{-1}), respectively.

extensive data set by Breger et al. (1999), Breger (2000b), and Breger et al. (2008) led to the discovery of a complex pulsation pattern consisting of 18 independent pulsation modes (Table 1). The main range of pulsation frequencies lies between 4 d^{-1} and 10 d^{-1}. Additional combination frequencies have been detected in lower and higher frequency ranges. Almost all modes show variations in amplitude and frequency that occur over several years and decades. Amplitude variations have been observed in many δ Sct stars. With sufficient frequency resolution, modes with varying amplitude and phase can be resolved as two close frequencies that produce a beating pattern (Breger & Bischof 2002; Breger & Pamyatnykh 2006). Correlations between the amplitude and phase shifts can confirm a beating of two close, intrinsic modes as opposed to true amplitude variability of a single mode. For 4 CVn the frequencies 6.1170 d^{-1} and 6.1077 d^{-1} are confirmed to be intrinsic modes producing amplitude variations and phase shifts through beating (Breger 2010). However, for frequencies with amplitude and phase variability on timescales longer than one year, the coverage of the beating cycle is incomplete. Thus, it cannot be ruled out that they are single modes with true amplitude variability.

Mode identification can be achieved by interpretation of spectroscopic LPVs. The expansion and contraction of the star and displacements of stellar-surface elements caused by the oscillations lead to periodic Doppler shifts in the profiles of absorption lines. By comparing the observed properties of LPVs to theoretical predictions, the harmonic degree ℓ and the azimuthal order m of the mode can be derived. Moreover, fitting with synthetic line profiles allows the determination of other stellar parameters and line-profile parameters, such as the projected rotational velocity $v_{\rm eq} \sin i$, and the inclination i (the angle between the pulsation axis and the line of sight; we assume that the pulsation axis coincides with the rotation axis). Unlike brightness or radial velocity, which are values integrated over the stellar surface, LPVs are less prone to partial cancelation effects and therefore allow for the detection of high-degree modes (for details see Aerts et al. 2010, Chap. 6).

Spectroscopic data was gathered at the McDonald Observatory in Texas, USA, from January 2008 until June 2011 (see Sect. 2). Preliminary results of the frequency analysis and mode identification of the season of 2008 were published by Castanheira et al. (2008). They assigned ℓ and m values to five different modes previously detected in photometry, summarized in Table 1. No high-degree modes were found. Furthermore, they measured $v_{\rm eq} \sin i \geq 120$ km s^{-1} for 4 CVn.

A subsequent analysis by Breger (2010) revealed correlations between the frequency variations and the azimuthal orders of the modes. While the prograde modes of 4 CVn show an increasing frequency followed by a decline after the year 1991, its retrograde modes have a decrease in frequency with a rising value after 1991. Radial modes, on the other hand, show very little or no frequency variations. Breger (2010) interpreted this contrary behavior of prograde and retrograde modes as a change in rotational splitting.

For this paper we analyzed the complete data set of spectroscopic observations. First of all, we discovered the star to be a spectroscopic binary. After orbital subtraction, we performed mode identification by applying the Fourier-parameter fit method (Zima 2006) to the LPVs present in metal absorption lines in the 4 CVn spectrum (see Fig. 1). Additionally, we present an abundance analysis and confirm the solar-like metallicity of the star.

2. Data and observations

The Sandiford Échelle Spectrograph (McCarthy et al. 1993) is an instrument mounted on the 2.1 m Otto-Struve Cassegrain

Table 2. Observation log of obtained spectroscopy of 4 CVn.

Season	Start date	End date	Nights	N
2008	2008-Jan.-19	2008-May-20	33	874
2010	2010-Feb.-18	2010-May-26	33	767
2011	2010-Dec.-14	2011-Jun.-21	20	488
Total	2008-Jan.-19	2011-Jun.-21	86	2129

Notes. Nights denotes the number of nights observed in each specific year; N is the number of scientific spectra taken of 4 CVn. Not all spectra were used in the analysis because of cosmic-ray hits or very low S/N.

Table 3. Orbital parameters of 4 CVn.

$P_{\rm orb}$ (days)	124.44 ± 0.03
T (JD)	$2\,454\,605 \pm 10.3$
e	0.311 ± 0.003
ω (deg)	70.2 ± 0.7
K_1 (km s^{-1})	13.24 ± 0.05
γ (km s^{-1})	-10.44 ± 0.03
Rms (km s^{-1})	2.8

reflector telescope at the McDonald Observatory, Texas, USA. It has a resolving power of $R = 60\,000$ and is therefore ideally suited to observe the relatively bright star 4 CVn ($V = 6.04$ mag) with a high signal-to-noise ratio (S/N) and a high spectral resolution. Depending on the atmospheric conditions we chose an integration time of 600–900 s, leading to a mean S/N of ~200 at a temporal resolution of 4% and 10% for the two main modes present in the photometric data, $\nu_1 = 8.594$ d^{-1} and $\nu_2 = 5.048$ d^{-1}, respectively (see Table 1). The instrument provides a continuous wavelength coverage in the observed range of 4200 Å to 4700 Å. In total, 2129 spectra were obtained throughout 86 nights in the period from January 2008 until June 2011 (see Table 2) leading to a time span of $\Delta T = 1248$ d and thus to a frequency resolution of $1/\Delta T = 0.0008$ d^{-1}. For precise wavelength calibration, comparison frames of a Th-Ar lamp were obtained after each exposure.

Standard IRAF routines for the reduction of échelle spectra were used to carry out the data reduction and wavelength calibration. Subsequently, the spectra were normalized in a similar manner to that described by Pápics et al. (2012), i.e., by fitting a cubic spline to manually chosen continuum points. They were then cut around a suitable line for further analysis. This line, an absorption feature of Fe II at 4508.288 Å, was carefully chosen from the available spectral range, as explained below.

2.1. Line selection

Certain criteria have to be fulfilled for the selection of an absorption line for the analysis of the LPVs, such as a sufficient depth and sharpness. For sharp lines, the pulsational broadening is dominant over other line-broadening mechanisms across the whole profile. It is also important that the line is unblended and does not overlap with any other atomic line. Metal lines are therefore better suited for mode identification from LPVs than hydrogen or helium lines (for more details see Aerts et al. 2010, Chap. 6). Different spectral lines originate from different layers in the atmosphere and thus probe different pulsation modes. Therefore, the signatures of the oscillations might be smeared out in the line profiles of blended lines. Moreover, the displacement of the line-forming regions by the pulsations leads to slight variations of the local temperature, which in turn lead to equivalent width (EW) variations. This will affect the outcome of the mode identification and has to be taken into account.

Castanheira et al. (2008) found $v_{\rm eq} \sin i \geq 120$ km s^{-1} for 4 CVn, which means that the star is a moderately fast rotator. This aggravates the situation of dense blue spectra of F stars with only very small continuum regions, as each absorption line is rotationally broadened. To select suitable lines for our study, we calculated an atmospheric model with effective temperature $T_{\rm eff} = 6800$ K, surface gravity $\log g = 3.32$, and solar metallicity (Breger & Pamyatnykh 2002; Lenz et al. 2010) using the LLMODEL code (Shulyak et al. 2004). With the SYNTHV (Tsymbal 1996) code we computed a synthetic spectrum and checked each line separately. The Fe II line around 4508.288 Å is the only line that is unblended except for two contributions in the line wings of Ti II at 4506.743 Å (27.2% of the line depth of Fe II) and Fe I at 4509.735 Å (39.8%). The positions of the two blending features are marked by vertical, dashed lines in Fig. 1.

Additionally, Castanheira et al. (2008) used another Fe II line around 4549.474 Å for mode identification of the 2008 data set of 4 CVn in their analysis. We refrained from using this line because it turned out to be heavily blended by at least five other absorption features, of which Fe I at 4549.466 Å and Ti II at 4549.617 Å give the strongest contribution to this line blend.

3. Binarity and radial velocity variations

After the spectra were corrected for the barycentric velocity shift, a dominant non-sinusoidal variation was visible in the first moment of the line, which represents the radial velocity (for a definition, see Aerts et al. 1992). This periodicity can be explained by a binary component and the movement of the primary around the center of mass of the system. No spectral features of the secondary could be detected in the data. This is further discussed in Sect. 4.

Since the first moment of the line depends somewhat on the wavelength range within which it is calculated, we created five different data sets with different dispersion ranges. We then fitted a Keplerian orbit to each data set. The best solution and errors of the parameters were estimated with a Markov chain Monte Carlo (MCMC) method implemented in the package `emcee` (Foreman-Mackey et al. 2013). To account for the scatter due to pulsations, we assumed an uncertainty of $\sigma_{\rm RV} = 2.8$ km s^{-1} (the rms value of the residuals after subtraction of the binary model, see Table 3) for each radial velocity measurement. To account for the dependence of the radial velocities on the dispersion range, we fitted all five data sets combined. All five models are consistent within the uncertainties of each solution. Figure 2 shows the orbital model fitted to the radial velocities obtained from the dispersion range -128.0 km s^{-1} to 106.0 km s^{-1} and the residuals after subtraction of the mean orbit. The results are shown in Table 3.

Because of the binary motion of the pulsating star we expect the frequencies to show a periodic shift at the base of the orbital period (for an explanation of the Doppler shift of oscillation frequencies, see Shibahashi & Kurtz 2012). For the observed photometric frequencies a shift of ~0.0002 d^{-1} to ~0.0004 d^{-1} can be estimated. Since the analyzed data set has a frequency resolution of 0.0008 d^{-1}, we cannot resolve the expected frequency shifts caused by the binary motion. We also did not detect a variation based on the orbital period of the times of maxima in an (O–C) diagram of the first moment.

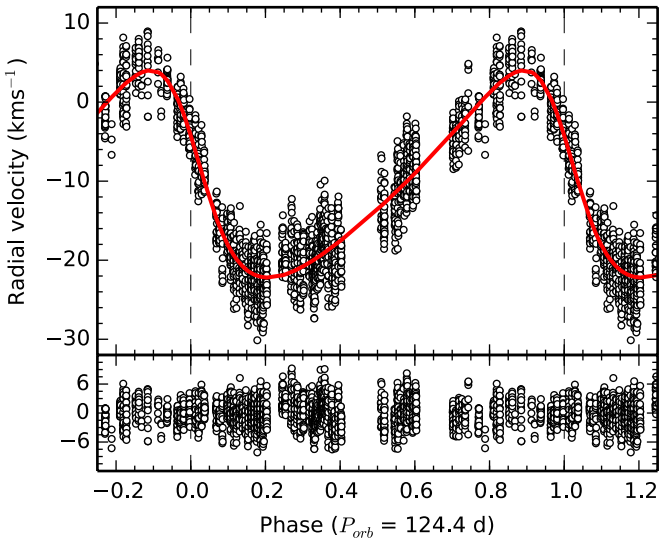

Fig. 2. *Upper panel*: observed radial velocities (open circles) fitted with the orbital model (solid line) with the parameters displayed in Table 3 and phased with the orbital period $P_{\rm orb}$ = 124.4 d. *Lower panel*: residuals after subtracting the binary model with an rms of 2.8 km s^{-1}. The pulsation signal (see Table 6) is visible on top of the variation due to binarity and remains present in the residuals. The vertical, dashed lines mark the beginning and the end of one phase.

From the mean binary orbit, a correction value was calculated for each spectrum to shift the data to the reference frame of the primary. The frequency analysis and mode identification of the pulsations was subsequently performed on the data corrected for the binary motion.

4. Revision of fundamental parameters

Since the data gathered at McDonald Observatory are limited in wavelength range, we obtained additional observations with the HERMES spectrograph (Raskin et al. 2011), a high-resolution spectrograph (R = 85 000) mounted at the 1.2 m Mercator telescope at La Palma, Spain. We obtained three spectra equally spread over the night of 3 February 2013. The reduction was performed by the HERMES pipeline and normalization was done in the same way as for the McDonald spectra, i.e., by fitting a cubic spline to the continuum region (Pápics et al. 2012). We extracted a wavelength range of 4500 Å to 6000 Å from the data.

For the analysis of the average spectrum of 4 CVn, we used the GSSP program package (Tkachenko et al. 2012; Lehmann et al. 2011). The code relies on a comparison between observed and synthetic spectra computed in a grid of $T_{\rm eff}$, log g, micorturbulence ξ, metallicity [m/H], and $v_{\rm eq}$ sin i, and finds the optimum values of these parameters from a minimum in χ^2. Individual abundances of chemical elements are adjusted in the second step by fixing the metallicity to the above determined value but keeping the other atmospheric parameters free. The errors of measurement (1σ confidence level) are calculated from the χ^2 statistics using the projections of the hypersurface of the χ^2 from all grid points of all parameters onto the parameter in question. For a more detailed discussion on the estimation of the uncertainties, see Tkachenko et al. (2013a). Strong LPVs detected in the spectrum of 4 CVn, as well as possible contributions from the secondary component, are an additional source of uncertainties which are not taken into account in the spectral analysis. Our analysis is based on the grid of atmosphere models computed using the most recent version of the LLMODELS code (Shulyak et al. 2004). For the calculation of the synthetic spectra, we used the SYNTHV code (Tsymbal 1996), and information on atomic lines has been extracted from the Vienna Atomic Line Database (VALD, Kupka et al. 2000).

Table 4. Fundamental and atmospheric parameters of 4 CVn.

$T_{\rm eff}$ (K)	6875 ± 120^a
log g (dex)	3.30 ± 0.35^a
[m/H] (dex)	-0.05 ± 0.15^a
$v_{\rm eq}$ sin i (km s^{-1})	109 ± 3^a
ξ (km s^{-1})	4.00 ± 0.45^a
ST	F2 III–IV^a
π (mas)	10.51 ± 0.40
log $L/L_\odot$	1.47 ± 0.05^b
Radius ($R_\odot$)	3.7–4.1^b
Mass ($M_\odot$)	1.0–2.0^b

Notes. $^{(a)}$ Parameters derived via spectral analysis. $^{(b)}$ Parameters based on combined photometric and spectroscopic observations.

Table 5. Abundances of individual chemical elements of 4 CVn.

Element	Value dex	Sun dex	Element	Value dex	Sun dex
Fe	–4.69(15)	–4.59	Cr	–6.47(20)	–6.40
Mg	–4.41(25)	–4.51	Mn	–6.65(40)	–6.65
Ti	–7.24(30)	–7.14	Si	–4.41(40)	–4.53
Ni	–5.82(20)	–5.73	C	–3.64(40)	–3.65
Ca	–5.84(25)	–5.73	Ba	–9.52(50)	–9.87
			Sc	–8.57(50)	–8.99

Notes. Error bars are given in parentheses in terms of last digits. Solar values are those derived by Grevesse et al. (2007).

Table 4 lists the atmospheric parameters of 4 CVn we derived. The individual abundances of some chemical elements are given in Table 5. The spectral type and the luminosity class have been computed using an interpolation in the tables published by Schmidt-Kaler (1982). Figure 3 compares the observations with the best fit synthetic spectrum in a 300 Å wide wavelength range including the H$_\beta$ spectral line.

Moreover, we used the HIPPARCOS parallax of 10.51 mas (van Leeuwen 2007) in combination with 2MASS and Geneva photometry to compute the luminosity and the radius of the star. We used a grid-based method, which also includes interstellar reddening as a free parameter, as described by Degroote et al. (2011). By using the radius and the spectroscopic log g we are able to estimate the mass. We find an extinction $E(B-V)$ = 0.02 mag. Although this value is close to zero, adding extinction to the calculations is important for the consistency of our estimated parameters, mass and radius. The results of the photometric analysis are summarized in Table 4.

We also used the above analyzed observed spectrum to compute a mean profile with a high S/N by means of the least-squares deconvolution technique (LSD; Donati et al. 1997; Kochukhov et al. 2010). Figure 4 shows the LSD profile of 4 CVn, the line mask was pre-computed based on the parameters listed in Table 4. Besides clear bumps in the center of the profile (dip) of the star, there is also an indication of another broad spectral line at $RV \sim 280$ km s^{-1}. Whereas the former is connected to the intrinsic variability of the star in terms of low- and high-degree non-radial pulsations, the latter might be a signature of a (very) faint stellar companion.

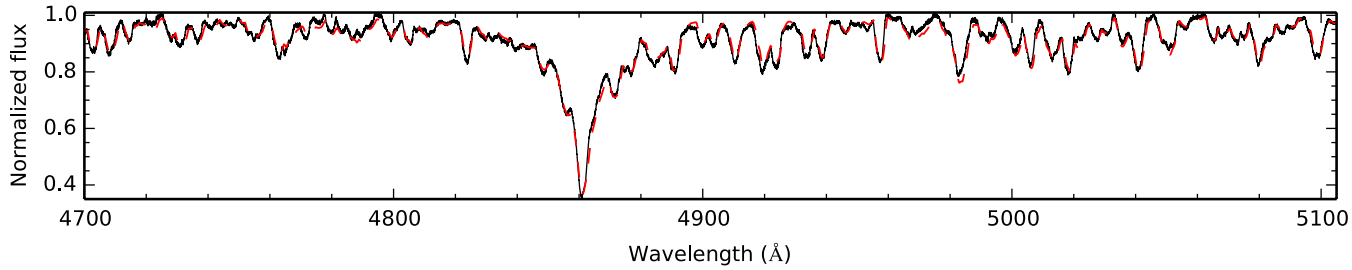

Fig. 3. Fit of the observed spectrum (solid) with a synthetic spectrum (dashed) computed using our optimized parameters (see Table 4).

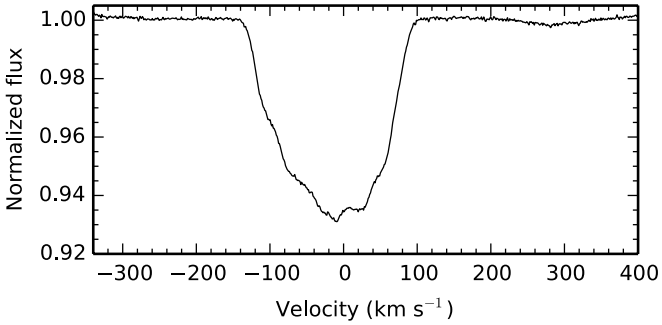

Fig. 4. Average line profile of 4 CVn computed by means of the LSD technique.

Given the measured semi-amplitude of the primary $K_1 = 13.24\,\mathrm{km\,s^{-1}}$ and the measured systemic velocity $\gamma = -10.44\,\mathrm{km\,s^{-1}}$, a radial velocity of $\sim$280 $\mathrm{km\,s^{-1}}$ of the secondary at orbital phase $\phi = 0.64$ would lead to a mass ratio of $q \leq 0.05$. The line strength of the spectral feature around $RV \sim 280\,\mathrm{km\,s^{-1}}$ in the LSD profile is $\sim$0.2%. If we assume a minimum contribution of $\sim$0.2% of the secondary to the system luminosity $\log L/L_\odot = 1.47$, we estimate $L_2 \sim 0.06\,L_\odot$, which corresponds to an early M-type main-sequence star of $\sim 0.6\,M_\odot$ (Carroll & Ostlie 2006, Appendix G). A mass ratio of $q \leq 0.05$ would then give a primary mass of $\sim 12\,M_\odot$, which is too massive given the observed spectral type F2III-IV.

The additional spectral contribution is so faint that it could also be an effect of continuum normalization. As the spectral lines of 4 CVn are broadened by fast rotation ($v_{\mathrm{eq}} \sin i = 109\,\mathrm{km\,s^{-1}}$), a continuum is not present everywhere in the wavelength range. Thus, inaccurate continuum normalization rather than a secondary signal is a more likely explanation for the spectral feature at $RV \sim 280\,\mathrm{km\,s^{-1}}$.

5. Frequency analysis

Before starting the analysis of the data we inspected each spectrum by eye. We rejected 93 observations, owing to weak cosmic-ray hits within the line or poor S/N, leaving 2036 good spectra (797 in 2008, 758 in 2010, and 481 in 2011). Since the periodogram of 4 CVn is characterized by amplitude variations on short and long timescales, we split the whole data set into three parts, and studied each season separately, otherwise the variability of the oscillation pattern would lead to disturbing side peaks in the Fourier spectra and to uncertainties between real frequency peaks and aliasing.

To search for significant periodicities in the LPVs we employed the Fourier-parameter fit method (FPF), which was developed by Zima (2006) as an advancement of the pixel-by-pixel method (Mantegazza 2000). It is implemented in the software package FAMIAS (Zima 2008). For each bin in the dispersion range of the line a Fourier transform is performed and a Lomb-Scargle periodogram (Lomb 1976; Scargle 1982) is calculated. An optimization of the mode parameters is done by applying a least-squares fitting algorithm to the original spectra, again, for each bin separately and thereby computing zero point, amplitude, and phase across the line profile. Subsequently, these parameters are used for mode identification (see Sect. 6). A Monte Carlo perturbation approach has been used to calculate the errors on the amplitudes, assuming a Gaussian distribution of the noise of the amplitude profiles. The S/N of each frequency is calculated from the mean periodogram, prewhitened with the significant frequency peaks. Thereby, the noise (σ_{res}) is calculated as the mean amplitude in a range of 10 $\mathrm{d^{-1}}$ (covering most of the frequency spectrum) around the frequency peak in the periodogram. We have adopted a significance criterion of $A > 4\sigma_{\mathrm{res}}$ (Breger et al. 1993). The results of our analysis are summarized in Table 6.

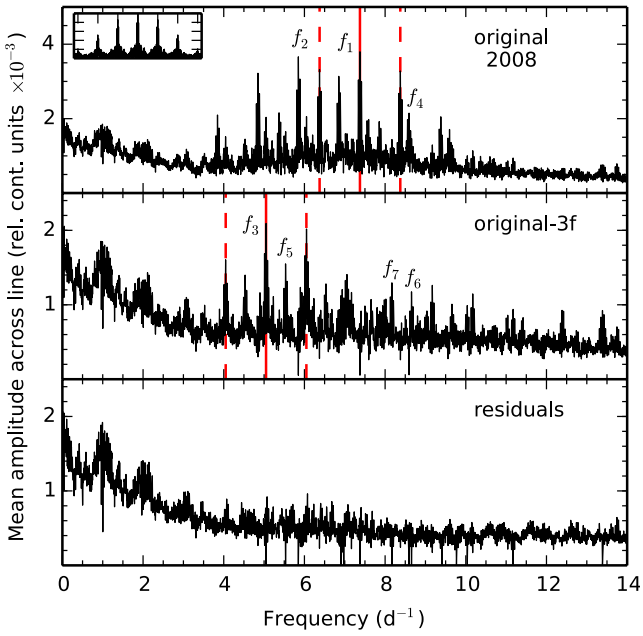

Fig. 5. Mean of the Lomb-Scargle periodograms per bin of the season of 2008. *From top to bottom*: mean Fourier spectra of the original data set, and after prewhitening of 3 and 14 frequencies, respectively. The red solid lines mark the highest peak in each periodogram, while the red dashed lines mark the respective one-day aliases. Highest peaks are $f_1 = 7.3764\ \mathrm{d^{-1}}$ (*upper panel*) and $f_3 = 5.0481\ \mathrm{d^{-1}}$ (*center panel*). The inset in the *upper panel* displays the spectral window for the 2008 data set.

Table 6. Spectroscopic frequencies and amplitudes of 4 CVn.

	Frequency d^{-1} ±0.0008	$A_{\text{whole set}}$ km s^{-1} ±0.009	A_{2008} km s^{-1} ±0.015	A_{2010} km s^{-1} ±0.014	A_{2011} km s^{-1} ±0.016
f_1	7.3764	0.953	0.95	0.98	1.00
f_2	5.8496	0.869	0.87	0.90	0.88
f_3	5.0481	0.550	0.48	0.53	0.59
f_4	8.5942	0.444	0.48	0.51	0.33
f_5	5.5315	0.389	0.38	0.39	0.44
f_6	8.6552	0.389	0.31	0.40	0.51
f_7	8.1687[a]	0.379	0.33	0.41	0.48
f_8	6.6801	whole set, 2010, 2011			
f_9	4.0743[a]	whole set, 2010, 2011[c]			
f_{10}	6.1171	whole set, 2010			
f_{11}	6.975[b]	2008			
f_{12}	10.1702[a]	whole set, 2010, 2011			
f_{13}	6.1910	whole set, 2011			
f_{14}	12.4244[a]	whole set, 2010, 2011			
f_{15}	9.4113[a]	whole set, 2008, 2010, 2011			
f_{16}	9.7684[a]	whole set, 2008, 2010			
f_{17}	10.0372[a]	whole set, 2008			
f_{18}	6.4030	whole set			
f_{19}	13.388[a]	2008			
f_{20}	10.016[a]	2011			

Notes. Amplitudes $A_{\text{whole set}}$ from the frequency analysis of the whole data set compared to the amplitudes of the different seasons A_{2008}, A_{2010}, and A_{2011}. The amplitudes have an average error of 0.009 km s^{-1} for the whole data set, and of 0.015, 0.014, and 0.016 km s^{-1} for the seasons 2008, 2010, and 2011, respectively. The frequency resolution $1/\Delta T$ is 0.0008 d^{-1} for the whole data set and 0.009, 0.01, and 0.005 d^{-1} for the seasons 2008, 2010, and 2011, respectively. [(a)] Frequencies not detected in previous photometric studies. [(b)] Photometric radial mode (Lenz et al. 2010). [(c)] Alias peak of frequency detected.

5.1. The Fe II line at 4508.288 Å

The increase in noise towards low frequencies in the periodograms (see Figs. 5–7) can be explained by instrumental effects or imperfect subtraction of the binary orbit. Given that the spectrograph is mounted at the telescope and not placed in a remote room where pressure and temperature could be kept constant to avoid spectral drift, some long-term variations are unavoidably present in the data. The high noise level can also be caused by instrumental noise and correlations of different noise sources. Residual variability on the basis of the binary orbit would cause frequency peaks around 0.008 d^{-1}. For these reasons, we discarded all low-frequency peaks below 2 d^{-1} as being not trustworthy. Furthermore, the daily gaps due to the night-day rhythm led to significant one-day aliasing, which is visible in the spectral window of each season (see inset in the top panels of Figs. 5–7 for seasons 2008, 2010, and 2011, respectively). To overcome these obstacles a prewhitening of each frequency was performed before carrying out another Fourier transform.

Figures 5–7 display the mean of the periodograms that were computed for each bin and for the seasons 2008, 2010, and 2011, respectively. Different stages of prewhitening are shown and the seven dominant frequencies are marked. We found six frequencies that are confirmed by photometric studies and are present in the periodograms of the whole data set and in all three seasons separately as well. These are f_1 = 7.3764 d^{-1}, f_2 = 5.8496 d^{-1}, f_3 = 5.0481 d^{-1}, f_4 = 8.5942 d^{-1}, f_5 = 5.5315 d^{-1}, and f_6 = 8.6552 d^{-1} (Breger et al., in prep.). Other photometrically significant frequencies could be detected in some seasons, while their amplitude was below the detection limit in other subsets. The frequency f_{11} = 6.975 d^{-1}, for example, could only be detected in 2008. Breger et al. (in prep.) confirm a rapid, steady decrease in amplitude for this frequency from 2008 to 2012. The frequencies f_8 = 6.6801 d^{-1}, f_{10} = 6.1171 d^{-1}, and f_{13} = 6.1910 d^{-1} also appear to be varying in amplitude, since they have only been detected in either the season of 2010 or 2011, or in both. However, the amplitude variabilities we detected for f_8, f_{10}, and f_{13} do not agree with the amplitudes derived from the photometric data set. Since these

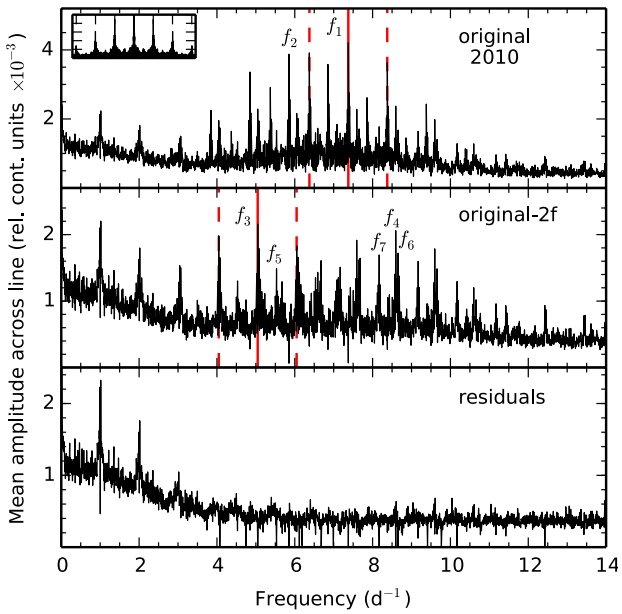

Fig. 6. Same as Fig. 5 for the season of 2010. *From top to bottom*: mean Fourier spectra of the original data set, and after prewhitening of 2 and 17 frequencies, respectively. The highest peaks marked by the red solid lines are f_1 = 7.3764 d^{-1} (*upper panel*) and f_3 = 5.0481 d^{-1} (*center panel*).

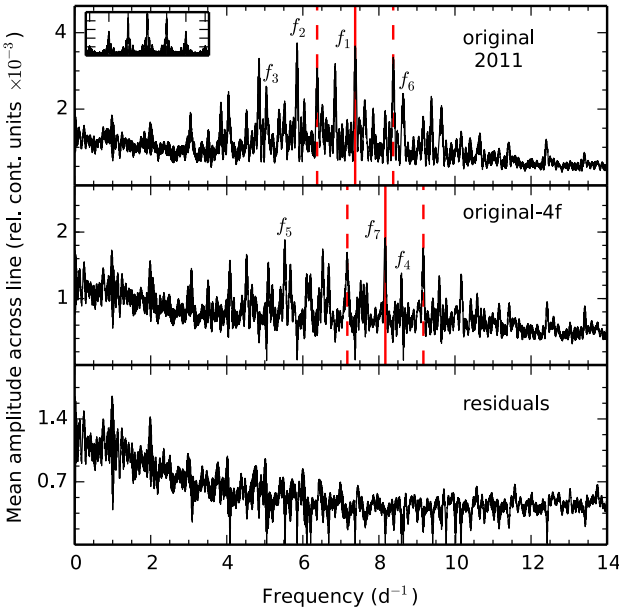

Fig. 7. Same as Fig. 5 for the season of 2011. *From top to bottom*: Fourier spectra of the original data set, and after prewhitening of 4 and 16 frequencies, respectively. The highest peaks marked by the red solid lines are f_1 = 7.3764 d^{-1} (*upper panel*) and f_7 = 8.1687 d^{-1} (*center panel*).

frequencies have a low S/N, their amplitude could also be below the detection limit in other seasons.

Additionally, we found several frequencies that were not detected in previous photometric studies by Breger et al. (1999), Breger (2000b), and Breger et al. (2008), among them f_7 = 8.1688 d^{-1}, f_9 = 4.0743 d^{-1}, f_{15} = 9.4113 d^{-1}, and f_{16} = 9.7684 d^{-1}. The frequency f_7 can be detected with a comparatively high amplitude ($A > 0.3$ km s^{-1}) in all sets and subsets. Frequencies f_9, f_{15}, and f_{16} have much lower amplitudes, and the amplitudes of f_9 and f_{16} even lie below the detection limit of seasons 2008 and 2011, respectively. The consistency of the detection in the separate seasons and the sufficient S/N for these frequencies in the merged data of the three seasons led us to the conclusion that they correspond to real oscillation frequencies. The fact that these frequencies were not detected in photometry suggests that they are either high-degree modes with $\ell \geq 2$ or are varying in amplitude and have reached detectable amplitudes in the last five years.

Breger et al. (1999) could identify peaks above 10 d^{-1} as combination frequencies of the main modes between 4 d^{-1} and 10 d^{-1}. The frequencies f_{12} = 10.1702 d^{-1}, f_{14} = 12.4244 d^{-1}, f_{17} = 10.0372 d^{-1}, f_{19} = 13.388 d^{-1}, and f_{20} = 10.016 d^{-1} lie in this high frequency range, but could not be confirmed to be combinations of any of the detected frequency peaks with $4 \leq f \leq 10$ d^{-1}. The amplitude and the phase profiles across the line of a mode offer an additional diagnostic to distinguish between noise peaks and real frequencies. If these profiles show a significant trend and not just random scatter, the frequency is likely to be a real pulsation mode. In Appendix A the amplitude and phase profiles across the line are displayed for the frequencies f_8 to f_{20}. While the amplitude profiles of f_{12}, f_{14}, f_{17}, f_{19}, and f_{20} are rather noisy, the phase profiles of these peaks do resemble those of real mode frequencies, i.e., increasing or decreasing from the blue to the red edge of the line. They were thus added to Table 6.

In order to test the influence of the line-cutting limits, we did a frequency analysis using different dispersion ranges for the Fe II line 4508.288 Å, as explained in Sect. 3. All different values of frequency and amplitude for all five dispersion ranges are consistent within the 1σ error bars.

5.2. Analysis of LSD profiles

As a result of the high rotation rate of the star, we only found one absorption line to be suitable for performing mode identification. In order to test the potential of using more information from the other spectral lines, we calculated LSD profiles for the McDonald spectra obtained in 2010 with the method by Kochukhov et al. (2010) and Tkachenko et al. (2013b). We made use of the line mask, which was computed for Sect. 4, to calculate a standard LSD profile from all the lines in the line mask, as well as an LSD profile of the Fe lines only, using the multi-profile technique, in order to take the blending of Fe-lines into account. Figures B.1–B.3 show the mean profile, the standard deviation, and a 2D color image of the LPVs, phase folded onto the frequency f_1 = 7.3764 d^{-1}, for the Fe II line at 4508.288 Å, the standard LSD profiles, and the Fe-LSD profiles, respectively.

The shape and depth of an LSD profile depends on the line mask used for the computation. As it can be considered an average of several lines (weak and strong lines of different elements), the depth will typically be less than that of a strong single line, such as Fe II at 4508.288 Å. In addition, the overall shape of the LSD profile can differ from that of a single line. All these effects can be seen in the figures in Appendix B. We note that the amplitude scales in Fig. B.1 (single Fe II line) are different from the amplitude scales in Fig. B.2 (standard LSD profiles) and Fig. B.3 (Fe-LSD profiles). The uneven structure in the continuum region in the lower panels of Figs. B.2 and B.3 is a consequence of the continuum normalization, which is complicated by the high $v_{\rm eq} \sin i$ = 109 km s^{-1} of 4 CVn. We did not detect any feature in the LSD profiles that is moving according to the orbital period and could be connected to the companion of 4 CVn.

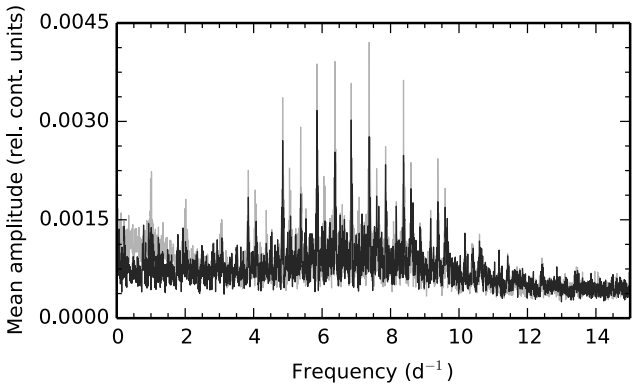

Fig. 8. Mean of the Lomb-Scargle periodogram per bin in the season of 2010 for the Fe II line 4508.288 Å (gray) and the standard LSD profiles for all lines in the line mask, rescaled to the depth of the Fe II line (black).

As already explained in Sect. 2.1, different lines can be more or less sensitive to stellar pulsations. It is therefore possible that the pulsation signal is smeared out in an LSD profile. This can affect the phase, but also the amplitude of the pulsation modes. Figure 8 depicts the mean amplitude spectra for the Fe II line 4508.288 Å (gray) and for the standard LSD profiles (black). In order to compare the two periodograms, we had to rescale the LSD profiles to match the amplitude of the Fe II line, as the pulsation amplitudes are expressed in units relative to the continuum of the line. The noise level in the periodogram of the rescaled LSD profiles is only lower in the low-frequency range and it contains less pulsation signal than the periodogram of the single line. This is reflected in the number of detected frequencies. While we were able to detect 14 significant ($A > 4\sigma_{\rm res}$) frequencies in the LPVs of Fe II (Table 6), we could only find 8 of them in the LPVs of the LSD profile. The frequencies detected in the LSD profiles had a lower S/N, and the amplitudes dropped by almost 30% for f_1 and by ~7% for f_2.

The results are similar for the LSD profiles based only on the Fe lines. The noise level in the mean periodogram of the Fe-LSD profiles is slightly higher than in the mean periodogram of the standard LSD profiles, since fewer lines were used for the computation of the profiles. Consequently, the amplitudes and S/N of the detected frequencies are even lower than the values found from the analysis of the standard LSD profiles.

As the LSD profiles do not yield any improvement to the single line, we conducted the further analysis on the Fe II line 4508.288 Å. It was already stressed by Aerts et al. (2010, Chap. 4) that line-profile analysis works best on one carefully selected, isolated line, if available.

6. Mode identification

6.1. Fourier-parameter fit method

During the frequency analysis (see Sect. 5) the observed Fourier parameters zero point Z_λ, amplitude A_λ, and phase ϕ_λ across

the line were obtained for each oscillation frequency. For mode identification the observed profiles are compared to theoretical profiles. Possible solutions can be compared by calculating a reduced χ^2. The theoretical values are computed from synthetic line profiles, which result from an integration over a surface grid divided into 10 000 segments. The intrinsic profile of each surface element is assumed to be Gaussian, and the local variations of flux arise from variations of temperature and surface gravity. Temperature variations, which lead to a varying EW, are neglected in a first approximation. Thus, we can also neglect the dependence of EW on temperature and assume a constant EW. The method is described in detail by Zima (2006, 2008, and references therein).

To obtain accurate mode identification, the FPF method requires the input of stellar parameters, such as mass, radius, metallicity, temperature, and surface gravity. Besides giving a solution for (ℓ, m), it also allows us to derive parameters of the line that are independent of pulsation, like, EW (only in first approximation), the width of the intrinsic Gaussian profile σ, and the velocity offset of the line center at 0 km s^{-1} dZ, which is a measure of radial velocity. Additionally, the inclination angle between pulsation axis and line of sight as well as $v_{\rm eq} \sin i$ can be derived.

We note that the method is most powerful when determining the m-values and not as powerful for the ℓ-values (Zima 2008).

6.2. Mode identification of f_1 = 7.3764 d^{-1} and f_2 = 5.8496 d^{-1}

Mode identification was carried out for the two dominant frequencies $f_1 = 7.3764$ d^{-1} and $f_2 = 5.8496$ d^{-1}. We folded the series of spectra on the phase of f_1 and f_2, respectively, and smoothed the LPVs in 50 phase bins. In this way we removed the signal of the several other p-modes which are excited to very low amplitudes and whose frequencies are hard to distinguish from noise and can therefore not be extracted from the data. Hence, we are able to treat the star as a mono-periodic pulsator during the mode identification. The zero point, amplitude, and phase profiles across the line obtained from the phase folded data set are displayed in Figs. 9 and 10 for f_1 and f_2, respectively.

We found the solution $(\ell_1, m_1) = (3, -2)$ for f_1. For f_2, mode identification was ambiguous; $(\ell_2, m_2) = (3, 3)$ and $(\ell_2, m_2) = (2, 2)$ are the best fits to f_2 depending on the stellar input parameters. However, other solutions cannot be excluded for both f_1 and f_2, since the χ^2 differs by only a few percent. Furthermore, we obtain a high χ^2 ($\chi^2 > 28$) for all ℓ and m combinations, which means that no solution provides a good fit to the observations. This will be discussed in Sect. 7. All results are summarized in Tables C.1–C.3. Figures C.1–C.6 show the observed amplitude and phase profile of f_1 fitted with the modes $(3, -2)$, $(3, -3)$, $(3, -1)$, $(2, -2)$, $(2, -1)$, and $(1, -1)$, respectively. The fits to the observed amplitude and phase profile of f_2 with the modes $(3, 3)$, $(3, 2)$, $(3, 1)$, $(2, 2)$, $(2, 1)$, and $(1, 1)$ are shown in Figs. C.7–C.12, respectively.

6.2.1. Line-profile parameters

Before fitting amplitude and phase across the line to identify the modes, the pulsation-independent line-profile parameters, $v_{\rm eq} \sin i$, EW, σ, and dZ are constrained by fitting the zero-point profile with a non-pulsating model. However, these parameters varied when fitting the pulsation modes and were therefore left as free parameters during the mode identification. The ranges within which the fits were computed are summarized in Table 7.

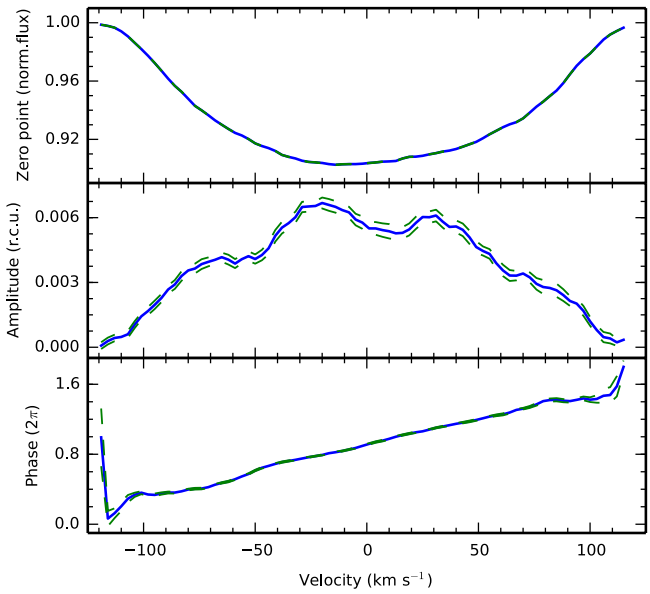

Fig. 9. Zero point (*upper panel*), amplitude (*center panel*), and phase (*lower panel*) across the line of the frequency f_1, calculated with the phase folded data set. Observations are shown as the blue solid line, while the errors of the observations are the green dashed lines.

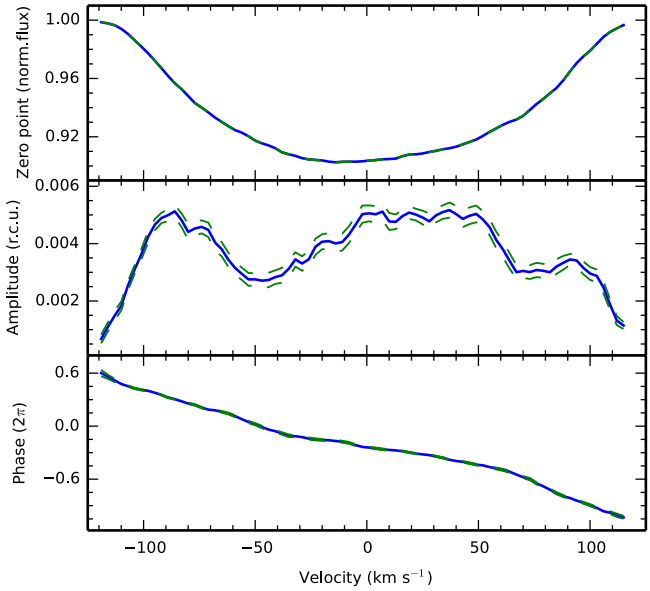

Fig. 10. Zero point (*upper panel*), amplitude (*center panel*), and phase (*lower panel*) across the line of the frequency f_2, calculated with the phase folded data set. The colors and lines have the same meaning as in Fig. 9.

6.2.2. Three sets of stellar input parameters

The photometric and spectroscopic analysis, presented in Sect. 4, suggests that the mass of 4 CVn lies between 1 $M_\odot$ and 2 $M_\odot$, while the radius is between 3.7 $R_\odot$ and 4.1 $R_\odot$. The effective temperature of the star $T_{\rm eff} = 6875 \pm 120$ K, the surface gravity $\log g = 3.3 \pm 0.35$ dex, and the metallicity is near solar.

Table 7. Line-profile parameters used for the mode identification of 4 CVn.

Central wavelength (Å)	4508.288
$v_{\rm eq} \sin i$ (km s^{-1})	106.0–107.3
EW (km s^{-1})	15.0–15.25
σ (km s^{-1})	8.0–9.5
dZ (km s^{-1})	−0.05–0.5

Notes. The ranges of the line-profile parameters contain the best fits of the different sets of stellar parameters and the frequencies f_1 and f_2.

Table 8. Stellar input parameters for the mode identification of 4 CVn.

	Set 1[a]	Set 2[a]	Set 3[b]
Mass ($M_\odot$)	2.0	1.5	2.4
Radius ($R_\odot$)	3.72	3.75	5.6
$T_{\rm eff}$ (K)	7050	6950	6800
$\log g$ (dex)	3.6	3.45	3.32
[m/H] (dex)	0	0	0
$v_{\rm crit}$ (km s^{-1})[c]	320.3	276.3	286.0
Inclination (deg)		23–90	

Notes. [(a)] Values based on our spectroscopic and photometric analysis (see Sect. 4). [(b)] Values based on Breger & Pamyatnykh (2002). [(c)] The critical velocity is given by $v_{\rm crit} = \sqrt{GM_*/R_{\rm e}}$.

Breger & Pamyatnykh (2002) computed a model with the 18 photometrically observed frequencies of 4 CVn, assuming $M = 2.4\ M_\odot$, $\log L/L_\odot = 1.76$, $T_{\rm eff} = 6800$ K, $\log g = 3.32$, $V_{\rm rot} = 82$ km s^{-1}, and solar metallicity. The luminosity of this model is a factor of 2 higher than our deduced value $\log L/L_\odot = 1.47 \pm 0.05$.

Since the stellar parameters are not well constrained, we calculated the mode identification for three different sets of parameters, which are summarized in Table 8. The values of set 1 and set 2 lie within the ranges of the results of our spectroscopic and photometric analysis, while the values for set 3 are based on the model by Breger & Pamyatnykh (2002). The inclination angle, i, was fitted within the range $23° \le i \le 90°$. We adopted a lower limit $i \sim 23°$ as it is the critical value where the star rotates at the break-up velocity ($v_{\rm crit} = \sqrt{GM_*/R_{\rm e}}$, where $R_{\rm e}$ is the equatorial radius; Townsend et al. 2004). The critical velocity $v_{\rm crit}$, which depends on the stellar mass and radius, is also given for each set in Table 8.

It is not possible to distinguish between the three sets of stellar parameters. The best solutions of all three sets lie within 10% of χ^2 and are therefore equally possible. For f_1, the best fitting (ℓ_1, m_1) combination is always a $(3, -2)$ mode. The solution for f_2, however, shows a dependence on the stellar input parameters and differs for the three different sets (see Tables C.1–C.3).

6.2.3. Inclination angle

For our computations, we assume that the pulsation axis coincides with the rotation axis. The inclination angle i is then the angle between this axis and the line of sight. It is thus not physically possible that f_1 and f_2 are observed at a different i. However, in Tables C.1–C.3 it can be seen that the value of i varies between the solutions for the different sets of stellar parameters and the two frequencies. This is also illustrated in Fig. 11 where (from top to bottom) the χ^2 distribution of i for sets 1–3 of the stellar parameters are displayed. The minimum χ^2 value is shown for each 3° bin in inclination for f_1 and f_2 in each

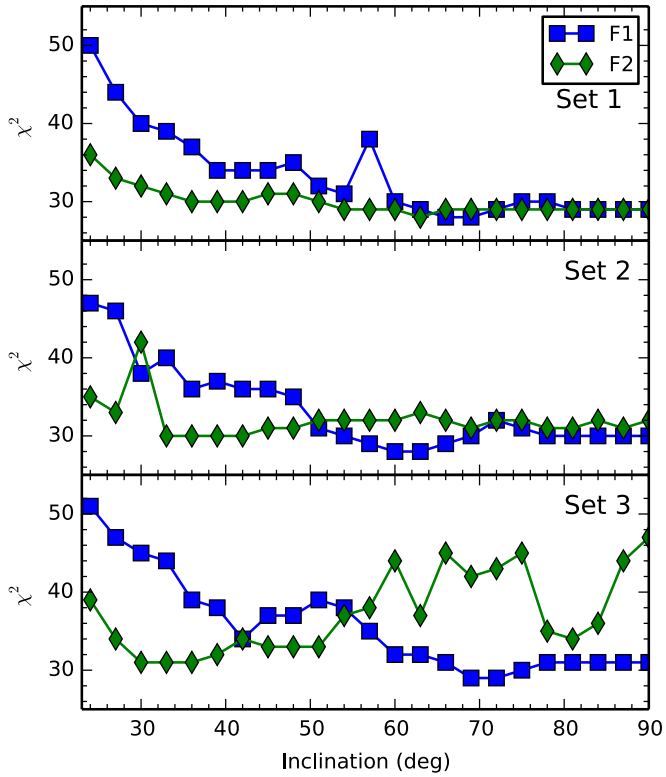

Fig. 11. χ^2 distribution of the inclination angle i for f_1 (blue squares) and f_2 (green diamonds) and for set 1 (*upper panel*), set 2 (*center panel*), and set 3 (*lower panel*) of the stellar parameters.

panel. For set 3 the frequencies f_1 and f_2 show an opposite behavior. While f_1 favors higher inclination values around ~60° to ~90°, mode identification for f_2 yields $i < 50°$. Set 1 and set 2 give a more consistent result for i, where f_1 and f_2 follow the same trend. On the other hand, there is also no clear minimum visible in χ^2, neither for f_1 nor for f_2 in any of the three sets. The inclination is highly degenerate with the degree ℓ and the order $|m|$ of the oscillation mode, as it determines the visibility of a certain mode. Mode identification was ambiguous for f_1 and f_2 and certain effects hamper us from drawing clear conclusions, as will be discussed in Sect. 7. Thus, we can also not find a consistent inclination for 4 CVn.

6.2.4. Temperature and equivalent-width variations

So far we have ignored variations of temperature in a first approximation and assumed a constant EW; thus, d(EW)/d($T_{\rm eff}$) = 0. To improve the fits of the amplitude and phase profiles we varied the parameter d(EW)/d($T_{\rm eff}$) and other parameters related to the temperature dependence of the flux variation; at first within a very broad range, and gradually narrowing down the range. However, the parameters did not converge and the minimum in χ^2 varied with each iteration, without improving the overall χ^2 significantly. The final solution therefore had to be calculated with d(EW)/d($T_{\rm eff}$) = 0, neglecting temperature variations.

6.3. Azimuthal order of the seven most-dominant frequencies

Mode identification has also been attempted for the frequencies f_3, f_4, f_5, f_6, and f_7. However, the amplitude of f_3 decreases by almost 40% compared to f_2 and the amplitudes of

Table 9. Identification of the azimuthal order for the seven dominant frequencies.

	Frequency d^{-1}	
f_1	7.3764	retrograde
f_2	5.8496	prograde
f_3	5.0481	retrograde or axisymmetric
f_4	5.5315	prograde
f_5	8.5942	prograde
f_6	8.6552	prograde
f_7	8.1688	high-degree, prograde

the other frequencies are even lower. Therefore, phase folding of the spectra on the respective frequencies and smoothing the LPVs in phase bins did not remove the signal of the two most-dominant frequencies sufficiently. Thus, a consistent mode identification cannot be achieved. However, as the FPF method is sensitive to phase, the slope of the phase profile across the line allows us to distinguish between *prograde* (i.e., a wave traveling in the direction of rotation; positive m, following the definition by Zima 2008), *retrograde* (negative m), and *axisymmetric* ($m = 0$) modes. Our results are given in Table 9.

We also attempted mode identification for $f_{12} = 6.975\ d^{-1}$. Our results do not contradict the solution presented in Lenz et al. (2010), who reported that it is a radial mode.

The very complex amplitude and phase profiles of f_7, i.e., containing many bumps, suggests that it is a high-degree mode, with $\ell \geq 3$. For modes with a high ℓ value, partial cancelation would lead to very low amplitudes in photometric observations, where the brightness variation integrated over the stellar disk is measured. This mode has not been detected in photometric data before, which supports our hypothesis of a high ℓ for f_7.

7. Discussion

7.1. Mode visibility and rotational splitting

The mode identification we attempted for the star 4 CVn yielded ambiguous results. The χ^2 statistics give several possible solutions for f_1 and f_2, depending on the stellar input parameters. For frequency $f_1 = 7.3764\ d^{-1}$ the best solution yields $\ell_1 = 3$ and for frequency $f_2 = 5.8496\ d^{-1}$, $\ell_2 = 2$ or $\ell_2 = 3$. Theory predicts that modes with degree $\ell = 3$ cancel out almost completely in photometric observations (Aerts et al. 2010, Chap. 6). However, both f_1 and f_2 were detected with significant amplitudes in photometric data (see Table 1), which contradicts the results of our mode identification. The solutions $(\ell_1, m_1) = (2, -2)$ and $(\ell_2, m_2) = (2, 2)$ would agree most closely with the current theory and our results.

We therefore tested the hypothesis that f_1 and f_2 are the outer parts of a rotationally split quintuplet. Rotational splitting (Ledoux 1951) describes the shift of frequencies of modes of same degree ℓ and different order $|m|$ ($0 \leq |m| \leq \ell$) due to the Coriolis force. It is dependent on $|m|$ and the rotational period of the star. With set 3 of the stellar parameters and $i > 80°$ it would be possible that we are observing rotational splitting in 4 CVn (see Table C.3 and Fig. 11).

7.2. Rotation rate

We conclude that 4 CVn rotates at a significant fraction of its critical velocity. We measured $v_{\rm eq} \sin i \simeq 106.7\ {\rm km\,s^{-1}}$ for the star. Thus, its equatorial velocity $v_{\rm eq}$ is at least ~33% of its critical velocity $v_{\rm crit}$. Since i and the stellar mass and radius are poorly constrained, it is possible that it rotates at up to almost ~70% of $v_{\rm crit}$. Tables C.1–C.3 provide the possible ranges of i and $v_{\rm eq}/v_{\rm crit}$.

Reese et al. (2013) showed that even a moderate rotation rate $v_{\rm eq}/v_{\rm crit} = 0.3$ has a large effect on the visibility of oscillation modes. While partial cancelation makes $\ell = 3$ modes almost not detectable in photometric data for slow rotation ($v_{\rm eq}/v_{\rm crit} \leq 0.2$), their amplitudes are as high as the amplitudes of modes with $\ell \leq 2$ if $v_{\rm eq}/v_{\rm crit} = 0.3$ (see Fig. 7 of Reese et al. 2013). This would mean that our results of $\ell = 3$ for f_1 and f_2 do not contradict the mode amplitudes observed in photometric light curves. However, fast rotation also alters the geometry of the modes (Reese et al. 2009). Since higher order effects of rotation are not yet included in the methodology for mode identification, this could be an explanation for the poor fits we obtained. If this is the case, the amplitude and phase profiles across the line, as well as the amplitude ratios of multicolor photometry would have to be revisited, with a methodology that includes the effects of rotation on the pulsation modes.

8. Summary

In this work, we analyzed the line-profile variations of the δ Sct star 4 CVn based on the spectroscopic observations obtained between January 2008 and June 2011 at McDonald Observatory, Texas, USA. We discovered that the star is the primary component of an eccentric binary system with an orbital period $P_{\rm orb} = 124.44 \pm 0.03$ d and eccentricity $e = 0.311 \pm 0.003$. No signal of the secondary could be detected in our data. The frequency analysis revealed 20 oscillation modes, 11 of which had already been detected in photometric data sets by Breger et al. (1999, 2008) and Breger (2000b).

By phase folding the series of spectra onto the two dominant frequencies f_1 and f_2 and smoothing the LPVs in phase bins, we removed the signal of other periodicities to prepare the data for mode identification. The best solution for frequency f_1 is an $(\ell_1, m_1) = (3, -2)$ mode, while the best solution for f_2 was either $(\ell_2, m_2) = (3, 3)$ or $(\ell_2, m_2) = (2, 2)$ depending on the stellar input parameters. For the calculations of the synthetic LPVs we used three different sets of stellar parameters:

1. $M = 2.0\ M_\odot$, $R = 3.72\ R_\odot$, $T_{\rm eff} = 7050$ K, $\log g = 3.6$, and [m/H] = 0.
2. $M = 1.5\ M_\odot$, $R = 3.75\ R_\odot$, $T_{\rm eff} = 6950$ K, $\log g = 3.45$, and [m/H] = 0.
3. $M = 2.4\ M_\odot$, $R = 5.6\ R_\odot$, $T_{\rm eff} = 6800$ K, $\log g = 3.32$, and [m/H] = 0.

Sets 1 and 2 are based on the spectroscopic and photometric analysis we performed to revise the stellar parameters. Set 3 is based on a model calculated by Breger & Pamyatnykh (2002). No set of stellar parameters can be excluded, based on the χ^2 statistics.

Relying on previous results by Castanheira et al. (2008), Breger (2010) claimed a relationship between the frequency variations of 4 CVn and the azimuthal order m of the modes, and especially the direction of the running wave (*retrograde*, *prograde*, or *axisymmetric/radial* modes). The FPF method is the most sensitive to the sign of m. Our results in Table 9 are in agreement with the directions of the waves used by Breger (2010).

The star is a fast rotator with $v_{\rm eq} \sin i \simeq 106.7\ {\rm km\,s^{-1}}$. Depending on the stellar input parameters and i (which could

not be constrained), the star is rotating at >33% of the critical velocity $v_{\rm crit}$. The higher order effects of rotation were not taken into account in our analysis, since they are not yet included in the methodology for mode identification.

A further limitation from the methodology is that unblended metal lines have to be used for mode identification. However, our observed spectral range (4500 Å to 4700 Å) is a very dense spectral region with many absorption lines and very little continuum for F stars, and almost all absorption lines are (heavily) blended. In an attempt to solve this problem, we calculated LSD profiles from the McDonald spectra obtained in the season 2010. We found that the pulsation signal is smeared out in the LSD profiles, as the number of significant oscillation modes detected in the LPVs of the LSD profiles is less than for the single Fe II line. The amplitudes and the S/N levels of these modes are also reduced significantly. To improve our analysis a method for identifying the modes in blended lines would have to be developed. In addition, observations in a wider spectral range could help solve the problem of blended lines. The lines that Zima et al. (2006) used for their analysis of the δ Sct star FG Vir lie outside the observed spectral range of the McDonald data. Observing a wider spectral range with a stable, high-resolution spectrograph would allow us to follow up on the additional spectral feature detected in the LSD profile of 4 CVn (see Fig. 4), and could possibly lead to identification of the origin of the latter.

Accurate mode identification of many observed frequencies is a crucial input for successful modeling of stellar oscillations. Analyses of LPVs are important as they can constrain the azimuthal order m of the pulsation modes. However, current shortcomings in the methodology prevent an unambiguous and accurate mode identification for 4 CVn. Including a complete description of rotation and the use of blended lines into mode-identification techniques will make this possible in the future.

Acknowledgements. This research has received funding from the Fonds zur Förderung der wissenschaftlichen Forschung (FWF), Austria P17441-N02, from the European Community's Seventh Framework Programme FP7-SPACE-2011-1, project number 312844 (SPACEINN), as well as from the Belgian Science Policy Office (Belspo, C90309: CoRoT Data Exploitation). It is partly based on observations made with the Mercator Telescope, operated on the island of La Palma by the Flemish Community, at the Spanish Observatorio del Roque de los Muchachos of the Instituto de Astrofísica de Canarias and obtained with the HERMES spectrograph, which is supported by the Fund for Scientific Research of Flanders (FWO), Belgium, the Research Council of KU Leuven, Belgium, the Fonds National Recherches Scientific (FNRS), Belgium, the Royal Observatory of Belgium, the Observatoire de Genève, Switzerland and the Thüringer Landessternwarte Tautenburg, Germany. S.B. is supported by the Foundation for Fundamental Research on Matter (FOM), which is part of the Netherlands Organisation for Scientific Research (NWO).

References

Aerts, C., de Pauw, M., & Waelkens, C. 1992, A&A, 266, 294
Aerts, C., Christensen-Dalsgaard, J., & Kurtz, D. W. 2010, Asteroseismology, 1st edn. (Springer), 866
Antoci, V., Handler, G., Campante, T. L., et al. 2011, Nature, 477, 570
Auvergne, M., Bodin, P., Boisnard, L., et al. 2009, A&A, 506, 411
Borucki, W. J., Koch, D., Basri, G., et al. 2010, Science, 327, 977
Breger, M. 2000a, in Delta Scuti and Related Stars, eds. M. Breger, & M. Montgomery, ASP Conf. Ser., 210, 3
Breger, M. 2000b, MNRAS, 313, 129
Breger, M. 2010, in Variable Stars, the Galactic halo and Galaxy Formation, eds. C. Sterken, N. Samus, & L. Szabados, 95
Breger, M., & Bischof, K. M. 2002, A&A, 385, 537
Breger, M., & Pamyatnykh, A. A. 2002, in Radial and Nonradial Pulsationsn as Probes of Stellar Physics, eds. C. Aerts, T. R. Bedding, & J. Christensen-Dalsgaard, IAU Colloq., 185, ASP Conf. Ser., 259, 388
Breger, M., & Pamyatnykh, A. A. 2006, MNRAS, 368, 571
Breger, M., Stich, J., Garrido, R., et al. 1993, A&A, 271, 482
Breger, M., Handler, G., Garrido, R., et al. 1999, A&A, 349, 225
Breger, M., Davis, K. A., & Dukes, R. J. 2008, Commun. Asteroseismol., 153, 63
Carroll, B. W., & Ostlie, D. A. 2006, An Introduction to Modern Astrophysics, 2nd edn. (Addison-Wesley), 1400
Castanheira, B. G., Breger, M., Beck, P. G., et al. 2008, Comm. Asteroseismol., 157, 124
Degroote, P., Acke, B., Samadi, R., et al. 2011, A&A, 536, A82
Donati, J.-F., Semel, M., Carter, B. D., Rees, D. E., & Collier Cameron, A. 1997, MNRAS, 291, 658
Foreman-Mackey, D., Hogg, D. W., Lang, D., & Goodman, J. 2013, PASP, 125, 306
Grevesse, N., Asplund, M., & Sauval, A. J. 2007, Space Sci. Rev., 130, 105
Grigahcène, A., Antoci, V., Balona, L., et al. 2010, ApJ, 713, L192
Kochukhov, O., Makaganiuk, V., & Piskunov, N. 2010, A&A, 524, A5
Kupka, F. G., Ryabchikova, T. A., Piskunov, N. E., Stempels, H. C., & Weiss, W. W. 2000, Balt. Astron., 9, 590
Ledoux, P. 1951, ApJ, 114, 373
Lehmann, H., Tkachenko, A., Semaan, T., et al. 2011, A&A, 526, A124
Lenz, P., Pamyatnykh, A. A., & Breger, M. 2010, in Variable Stars, the Galactic halo and Galaxy Formation, eds. C. Sterken, N. Samus, & L. Szabados, 83
Lomb, N. R. 1976, Ap&SS, 39, 447
Mantegazza, L. 2000, in Delta Scuti and Related Stars, eds. M. Breger, & M. Montgomery, ASP Conf. Ser., 210, 138
McCarthy, J. K., Sandiford, B. A., Boyd, D., & Booth, J. 1993, PASP, 105, 881
Murphy, S. J., Pigulski, A., Kurtz, D. W., et al. 2013, MNRAS, 432, 2284
Pápics, P. I., Briquet, M., Baglin, A., et al. 2012, A&A, 542, A55
Raskin, G., van Winckel, H., Hensberge, H., et al. 2011, A&A, 526, A69
Reese, D. R., MacGregor, K. B., Jackson, S., Skumanich, A., & Metcalfe, T. S. 2009, A&A, 506, 189
Reese, D. R., Prat, V., Barban, C., van 't Veer-Menneret, C., & MacGregor, K. B. 2013, A&A, 550, A77
Scargle, J. D. 1982, ApJ, 263, 835
Shibahashi, H., & Kurtz, D. W. 2012, MNRAS, 422, 738
Shulyak, D., Tsymbal, V., Ryabchikova, T., Stütz, C., & Weiss, W. W. 2004, A&A, 428, 993
Tkachenko, A., Lehmann, H., Smalley, B., Debosscher, J., & Aerts, C. 2012, MNRAS, 422, 2960
Tkachenko, A., Lehmann, H., Smalley, B., & Uytterhoeven, K. 2013a, MNRAS, 431, 3685
Tkachenko, A., Van Reeth, T., Tsymbal, V., et al. 2013b, A&A, 560, A37
Townsend, R. H. D., Owocki, S. P., & Howarth, I. D. 2004, MNRAS, 350, 189
Tsymbal, V. 1996, in , M.A.S.S., Model Atmospheres and Spectrum Synthesis, eds. S. J. Adelman, F. Kupka, & W. W. Weiss, ASP Conf. Ser., 108, 198
Uytterhoeven, K., Moya, A., Grigahcène, A., et al. 2011, A&A, 534, A125
van Leeuwen, F. 2007, A&A, 474, 653
Walker, G., Matthews, J., Kuschnig, R., et al. 2003, PASP, 115, 1023
Zima, W. 2006, A&A, 455, 227
Zima, W. 2008, Commun. Asteroseismol., 155, 17
Zima, W., Wright, D., Bentley, J., et al. 2006, A&A, 455, 235

Pages 12 to 17 are available in the electronic edition of the journal at http://www.aanda.org

Appendix A: Amplitude and phase profiles

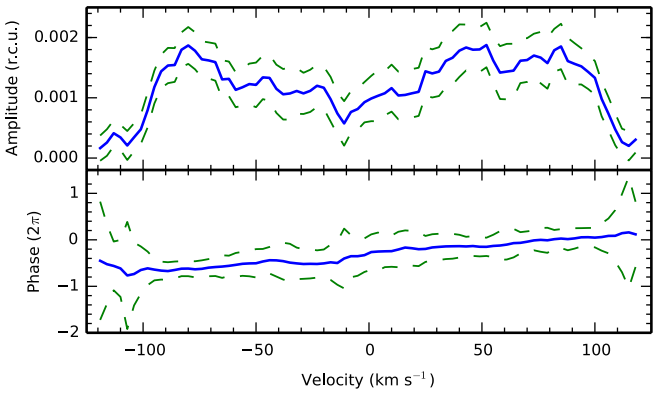

Fig. A.1. Amplitude (*upper panel*) and phase (*lower panel*) across the line for frequency f_8 = 6.6801 d^{-1}. Observations are shown as the blue solid line and errors of the observations are shown as the green dashed line.

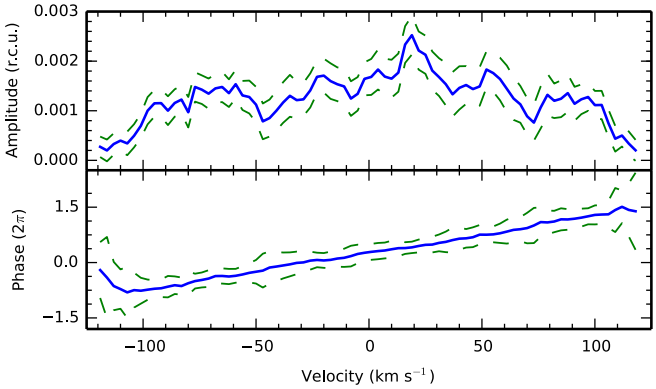

Fig. A.2. Same as Fig. A.1, but for frequency f_9 = 4.0743 d^{-1}.

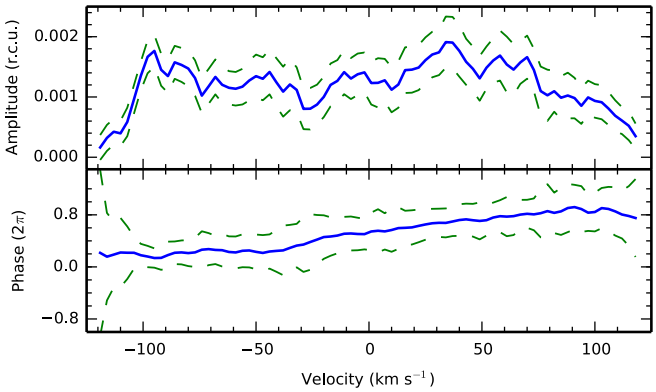

Fig. A.3. Same as Fig. A.1, but for frequency f_{10} = 6.1171 d^{-1}.

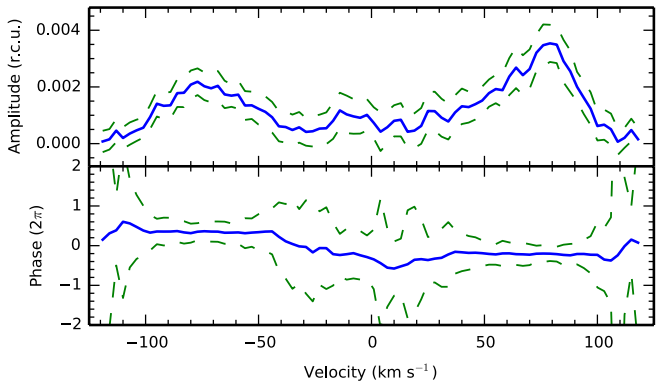

Fig. A.4. Same as Fig. A.1, but for frequency f_{11} = 6.975 d^{-1}.

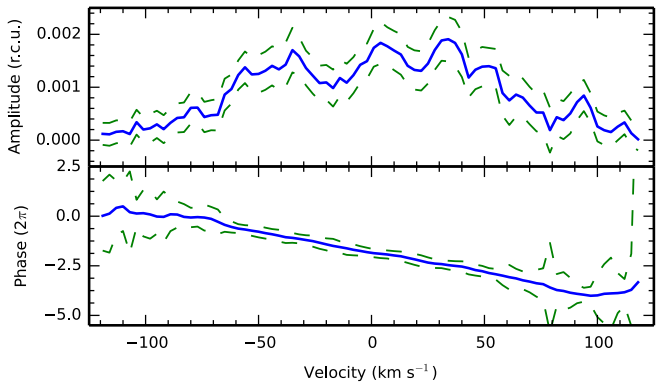

Fig. A.5. Same as Fig. A.1, but for frequency f_{12} = 10.1702 d^{-1}.

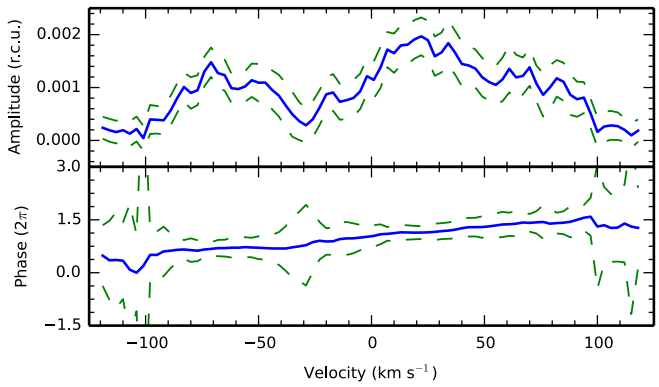

Fig. A.6. Same as Fig. A.1, but for frequency f_{13} = 6.1910 d^{-1}.

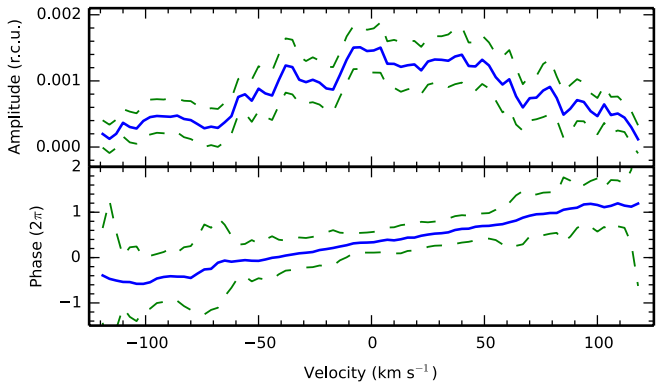

Fig. A.7. Same as Fig. A.1, but for frequency f_{14} = 12.4244 d^{-1}.

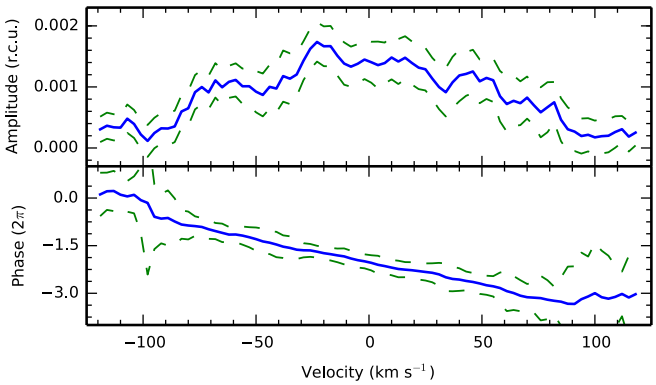

Fig. A.8. Same as Fig. A.1, but for frequency f_{15} = 9.4113 d^{-1}.

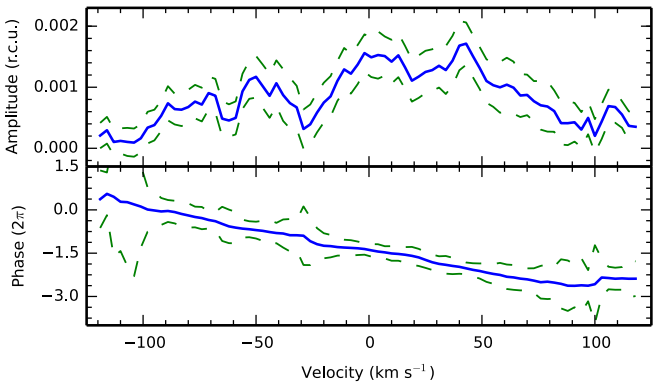

Fig. A.9. Same as Fig. A.1, but for frequency f_{16} = 9.7684 d^{-1}.

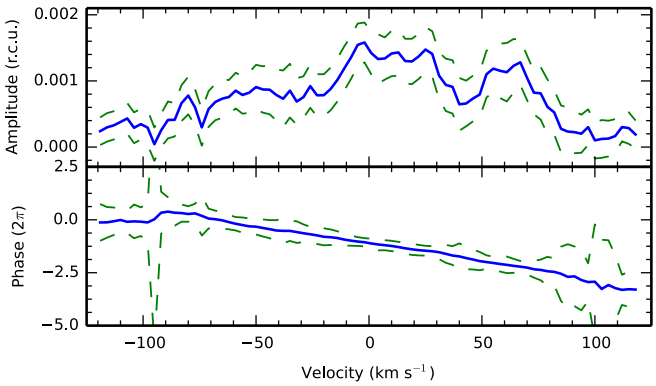

Fig. A.10. Same as Fig. A.1, but for frequency f_{17} = 10.0372 d^{-1}.

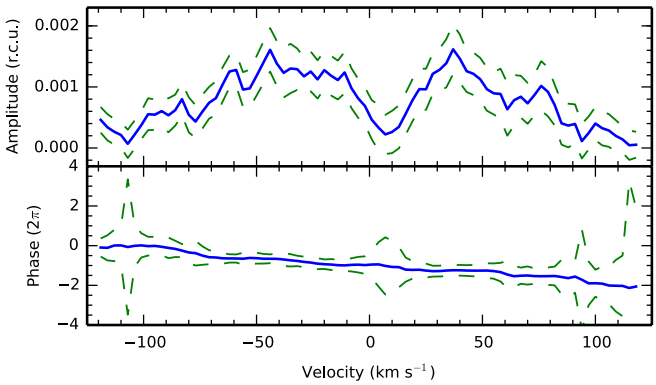

Fig. A.11. Same as Fig. A.1, but for frequency f_{18} = 6.4030 d^{-1}.

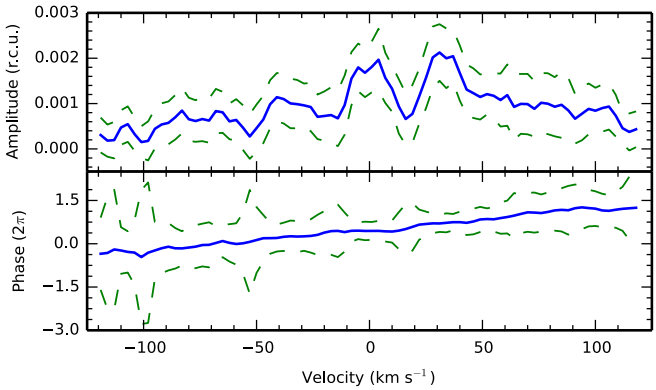

Fig. A.12. Same as Fig. A.1, but for frequency f_{19} = 13.388 d^{-1}.

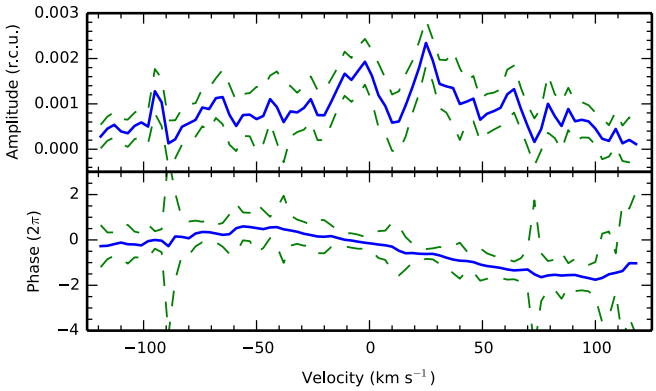

Fig. A.13. Same as Fig. A.1, but for frequency f_{20} = 10.016 d^{-1}.

Appendix B: Comparison of LSD profiles and single-line profiles

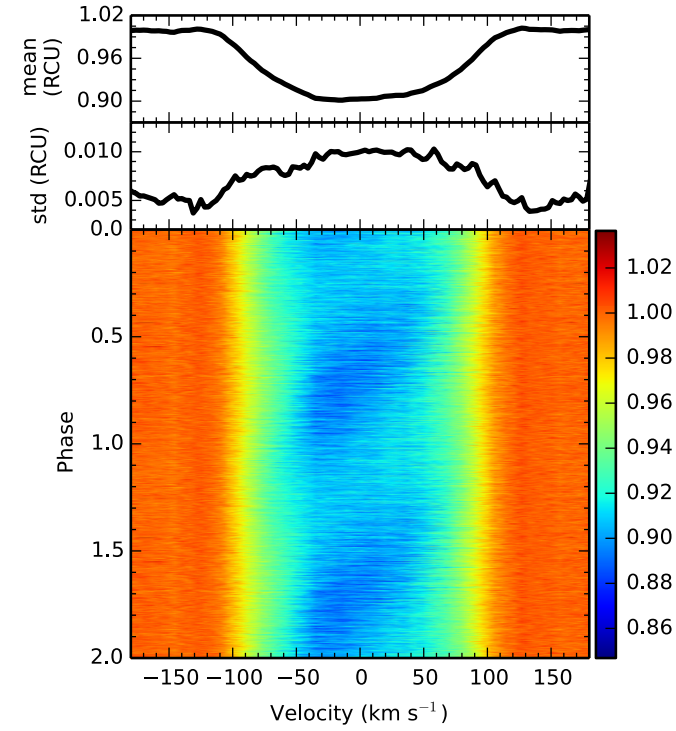

Fig. B.1. *Upper panel*: mean profile of the Fe II line at 4508.288 Å in the season 2010. *Center panel*: standard deviation of the Fe II line. *Lower panel*: color image of the LPVs of the Fe II line, phase folded on the frequency f_1 = 7.3764 d^{-1}. The amplitude is color coded and can be read from the color bar.

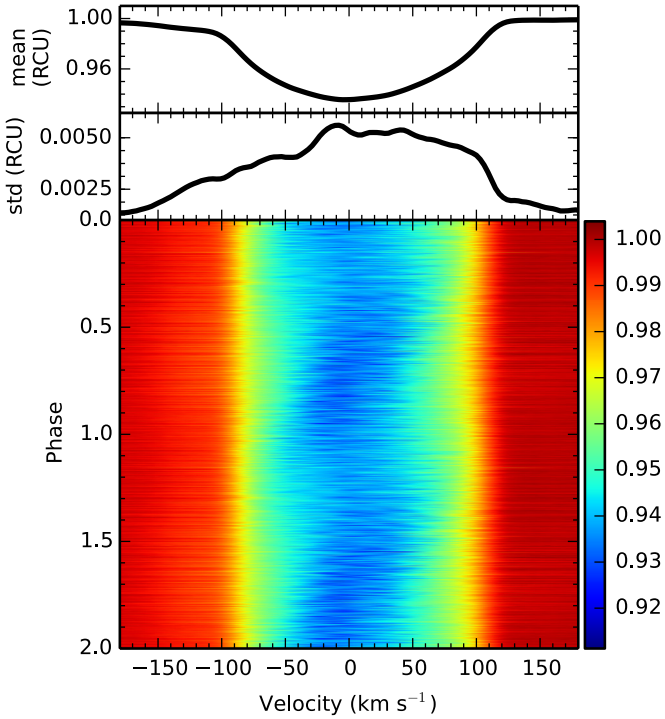

Fig. B.2. Same as Fig. B.1 for the standard LSD profiles calculated from all lines in the line mask.

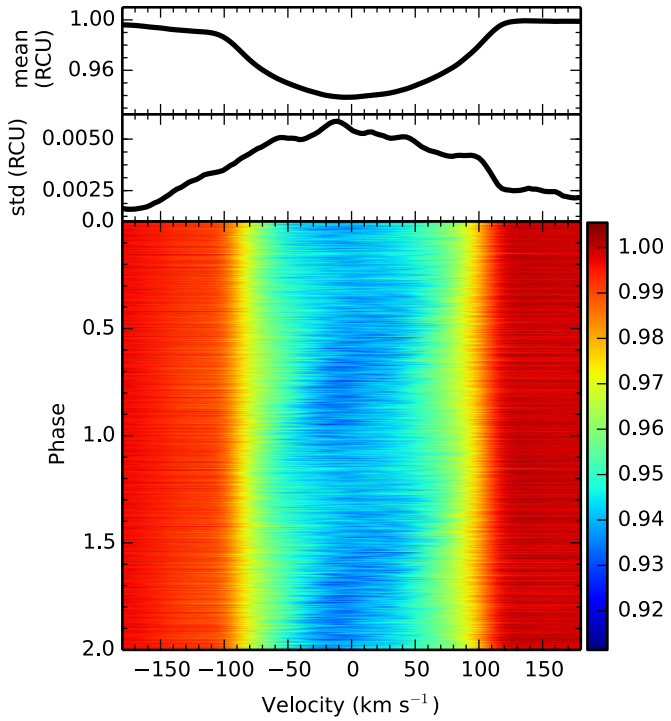

Fig. B.3. Same as Fig. B.1 for the LSD profiles calculated from all Fe lines in the line mask only.

Appendix C: Results of the mode identification of $f_1 = 7.3764\ \mathrm{d}^{-1}$ and $f_2 = 5.8496\ \mathrm{d}^{-1}$

Table C.1. Results of the mode identification using set 1 of the stellar parameters ($M = 2.0\ M_\odot$, $R = 3.72\ R_\odot$, $\log g = 3.6$, and $T_{\rm eff} = 7050$ K).

$f_1 = 7.3764\ \mathrm{d}^{-1}$						$f_2 = 5.8496\ \mathrm{d}^{-1}$					
(ℓ_1, m_1)	i (deg)	$v_{\rm eq} \sin i$ (km s^{-1})	$v_{\rm eq}$ (km s^{-1})	$v_{\rm eq}/v_{\rm crit}$	χ^2	(ℓ_2, m_2)	i (deg)	$v_{\rm eq} \sin i$ (km s^{-1})	$v_{\rm eq}$ (km s^{-1})	$v_{\rm eq}/v_{\rm crit}$	χ^2
(3, −2)	66.3	106.5	116.3	0.36	28.6	(3, 3)	61.0	106.9	122.2	0.38	29.0
(3, −3)	88.9	106.7	106.7	0.33	29.7	(3, 2)	36.2	106.8	180.8	0.56	30.8
(3, −1)	41.5	106.6	160.9	0.50	34.6	(3, 1)	51.5	106.6	136.2	0.43	35.3
(2, −2)	51.5	106.6	136.2	0.43	38.3	(2, 2)	44.1	106.8	153.5	0.48	39.6
(2, −1)	38.3	106.5	171.8	0.54	47.7	(2, 1)	35.1	106.7	185.6	0.58	65.6
(1, −1)	43.6	106.6	154.6	0.48	68.7	(1, 1)	24.6	106.7	256.3	0.80	68.3

Notes. The results are ordered by increasing χ^2. The critical velocity $v_{\rm crit} = 320.3$ km s^{-1}.

Table C.2. Results of the mode identification using set 2 of the stellar parameters ($M = 1.5\ M_\odot$, $R = 3.75\ R_\odot$, $\log g = 3.45$, and $T_{\rm eff} = 6950$ K).

$f_1 = 7.3764\ \mathrm{d}^{-1}$						$f_2 = 5.8496\ \mathrm{d}^{-1}$					
(ℓ_1, m_1)	i (deg)	$v_{\rm eq} \sin i$ (km s^{-1})	$v_{\rm eq}$ (km s^{-1})	$v_{\rm eq}/v_{\rm crit}$	χ^2	(ℓ_2, m_2)	i (deg)	$v_{\rm eq} \sin i$ (km s^{-1})	$v_{\rm eq}$ (km s^{-1})	$v_{\rm eq}/v_{\rm crit}$	χ^2
(3, −2)	61.5	106.7	121.4	0.44	28.7	(3, 3)	38.3	106.9	172.5	0.62	30.4
(3, −3)	90.0	106.8	106.8	0.39	30.5	(3, 2)	34.1	107.0	190.9	0.69	30.8
(3, −1)	43.0	106.7	156.5	0.57	36.0	(2, 2)	36.7	106.9	178.9	0.65	36.8
(2, −2)	58.3	106.8	125.5	0.45	38.5	(3, 1)	48.9	106.6	141.5	0.51	39.1
(2, −1)	43.0	106.6	156.3	0.57	47.7	(2, 1)	34.1	106.8	190.5	0.69	64.0
(1, −1)	43.6	106.7	154.7	0.56	69.1	(1, 1)	23.0	106.7	273.1	0.99	66.9

Notes. The results are ordered by increasing χ^2. The critical velocity $v_{\rm crit} = 276.3$ km s^{-1}.

Table C.3. Results of the mode identification using set 3 of the stellar parameters ($M = 2.4\ M_\odot$, $R = 5.6\ R_\odot$, $\log g = 3.32$, and $T_{\rm eff} = 6800$ K).

$f_1 = 7.3764\ \mathrm{d}^{-1}$						$f_2 = 5.8496\ \mathrm{d}^{-1}$					
(ℓ_1, m_1)	i (deg)	$v_{\rm eq} \sin i$ (km s^{-1})	$v_{\rm eq}$ (km s^{-1})	$v_{\rm eq}/v_{\rm crit}$	χ^2	(ℓ_2, m_2)	i (deg)	$v_{\rm eq} \sin i$ (km s^{-1})	$v_{\rm eq}$ (km s^{-1})	$v_{\rm eq}/v_{\rm crit}$	χ^2
(3, −2)	69.4	106.8	114.1	0.40	29.7	(2, 2)	31.5	107.0	204.8	0.72	31.6
(3, −3)	87.9	107.0	107.1	0.37	31.6	(3, 2)	79.4	106.5	108.3	0.38	34.0
(3, −1)	42.0	106.8	159.6	0.56	37.4	(3, 3)	23.0	107.2	274.4	0.96	43.8
(2, −2)	57.8	106.9	126.3	0.44	38.7	(3, 1)	40.9	107.0	163.4	0.57	44.3
(2, −1)	44.1	106.8	153.5	0.54	48.5	(2, 1)	30.9	107.0	208.4	0.73	57.4
(1, −1)	43.6	106.9	155.0	0.54	69.1	(1, 1)	23.0	107.0	273.8	0.96	61.7

Notes. The results are ordered by increasing χ^2. The critical velocity $v_{\rm crit} = 286.0$ km s^{-1}.

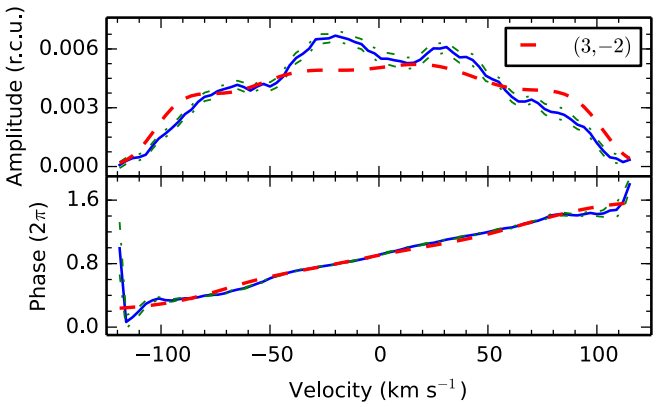

Fig. C.1. Fit of the amplitude (*upper panel*) and phase (*lower panel*) across the line of the frequency f_1 with a $(\ell, m) = (3, -2)$ mode. The observed profiles are calculated from the phase folded data set. Observations are shown as the blue solid line, the errors of the observations are shown as the green dash-dotted line, and the fit is shown as the red dashed line. The fit has a χ^2 of 28.6.

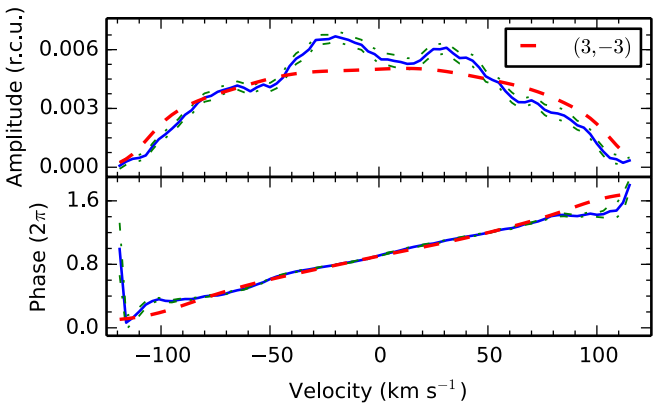

Fig. C.2. Same as Fig. C.1, but with a $(\ell, m) = (3, -3)$ mode. The fit has a χ^2 of 29.7.

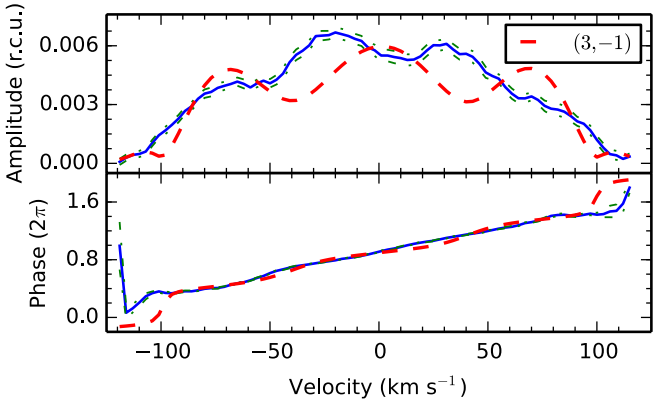

Fig. C.3. Same as Fig. C.1, but with a $(\ell, m) = (3, -1)$ mode. The fit has a χ^2 of 34.6.

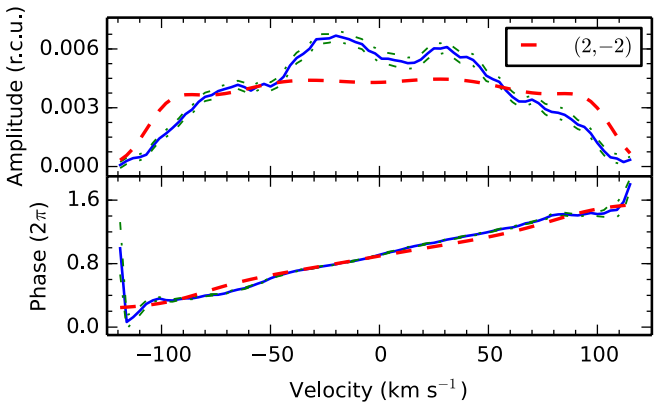

Fig. C.4. Same as Fig. C.1, but with a $(\ell, m) = (2, -2)$ mode. The fit has a χ^2 of 38.3.

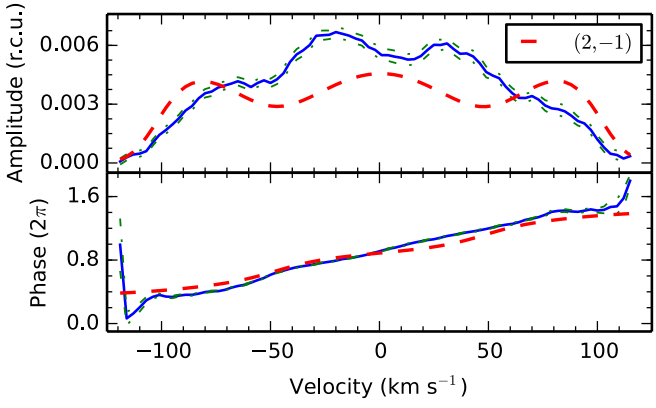

Fig. C.5. Same as Fig. C.1, but with a $(\ell, m) = (2, -1)$ mode. The fit has a χ^2 of 47.7.

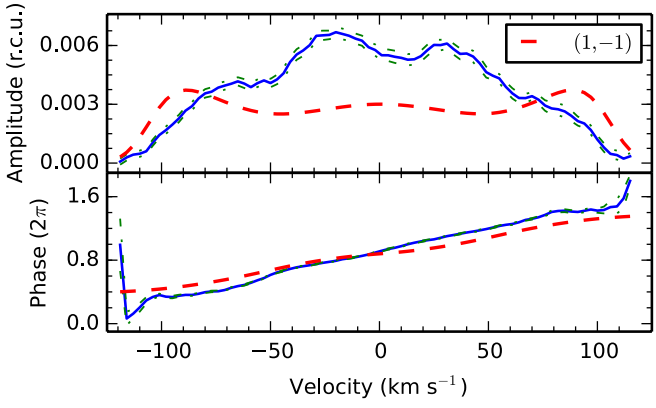

Fig. C.6. Same as Fig. C.1, but with a $(\ell, m) = (1, -1)$ mode. The fit has a χ^2 of 68.7.

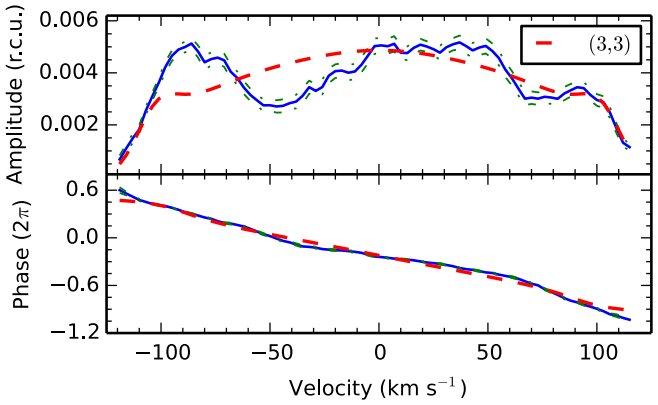

Fig. C.7. Fit of the amplitude (*upper panel*) and phase (*lower panel*) across the line of the frequency f_2 with a $(\ell, m) = (3, 3)$ mode. The observed profiles are calculated from the phase folded data set. Observations are shown as the blue solid line, the errors of the observations are shown as the green dash-dotted line, and the fit is shown as the red dashed line. The fit has a χ^2 of 29.

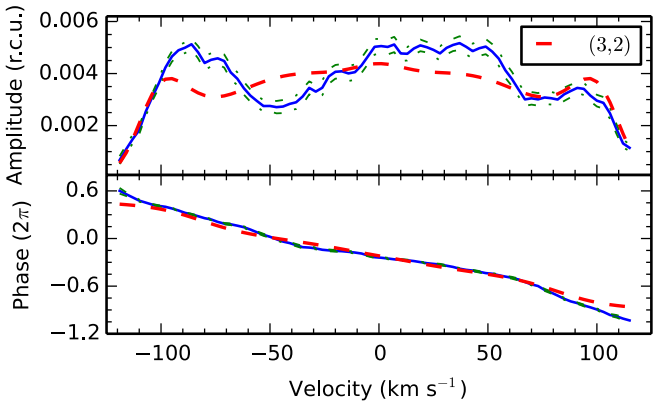

Fig. C.8. Same as Fig. C.7, but with a $(\ell, m) = (3, 2)$ mode. The fit has a χ^2 of 30.8.

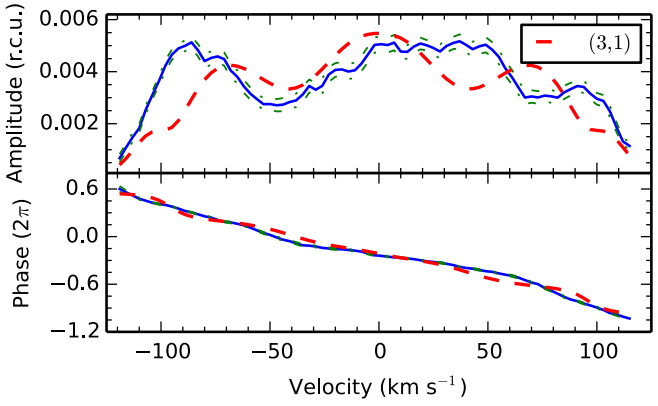

Fig. C.9. Same as Fig. C.7, but with a $(\ell, m) = (3, 1)$ mode. The fit has a χ^2 of 35.3.

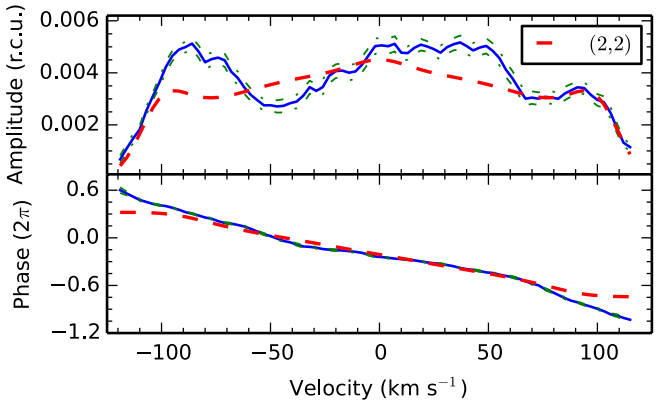

Fig. C.10. Same as Fig. C.7, but with a $(\ell, m) = (2, 2)$ mode. The fit has a χ^2 of 39.6.

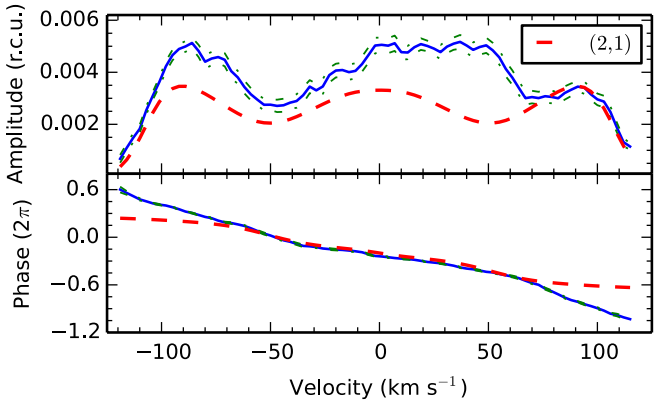

Fig. C.11. Same as Fig. C.7, but with a $(\ell, m) = (2, 1)$ mode. The fit has a χ^2 of 65.6.

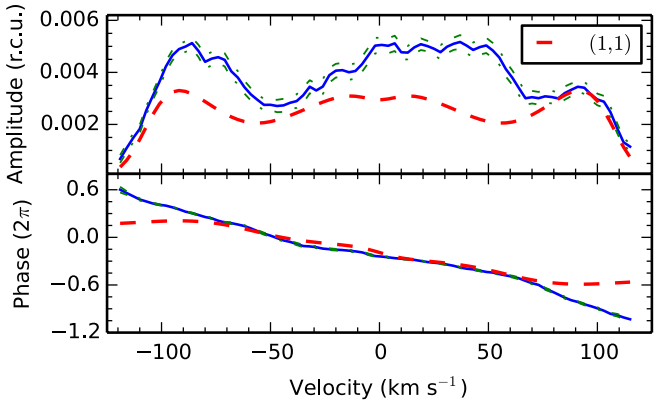

Fig. C.12. Same as Fig. C.7, but with a $(\ell, m) = (1, 1)$ mode. The fit has a χ^2 of 68.3.